

Control of spatiotemporal activation of organ-specific fibers in the swine vagus nerve by intermittent interferential current stimulation

Received: 10 October 2024

Accepted: 17 April 2025

Published online: 13 May 2025


 Check for updates

Nicolò Rossetti^{1,7}, Weiguo Song^{2,7}, Philipp Schnepel^{1,7}, Naveen Jayaprakash², Dimitrios A. Koutsouras¹, Mark Fichman¹, Jason Wong², Todd Levy², Mohamed Elgohary², Khaled Qanud², Alice Giannotti³, Mary F. Barbe⁴, Frank Liu Chen⁴, Geert Langereis¹, Timir Datta-Chaudhuri^{2,5,6}, Vojkan Mihajlović¹ & Stavros Zanos^{1,2,5,6} 

Vagus nerve stimulation (VNS) is emerging as potential treatment for several chronic diseases. However, limited control of fiber activation, e.g., to promote desired effects over side effects, restricts clinical translation. Towards that goal, we describe a VNS method consisting of intermittent, interferential sinusoidal current stimulation (i²CS) through multi-contact epineural cuffs. In experiments in anesthetized swine, i²CS elicits nerve potentials and organ responses, from lungs and laryngeal muscles, that are distinct from equivalent non-interferential sinusoidal stimulation. Resection and micro-CT imaging of a previously stimulated nerve, to resolve anatomical trajectories of nerve fascicles, demonstrate that i²CS responses are explained by activation of organ-specific fascicles rather than the entire nerve. Physiological responses in swine and activity of single fibers in anatomically realistic, physiologically validated biophysical vagus nerve models indicate that i²CS reduces fiber activation at the interference focus. Experimental and modeling results demonstrate that current steering and beat and repetition frequencies predictably shape the spatiotemporal pattern of fiber activation, allowing tunable and precise control of nerve and organ responses. When compared to equivalent sinusoidal stimulation in the same animals, i²CS produces reduced levels of a side-effect by larger laryngeal fibers, while attaining similar levels of a desired effect by smaller bronchopulmonary fibers.

Neural signaling through the vagus nerve is essential for physiological homeostasis through autonomic reflexes¹ and is implicated in the pathogenesis of several chronic brain, cardiopulmonary, gastrointestinal, and inflammatory diseases². For those reasons, the vagus nerve has emerged as a target for therapeutic neuromodulation, with

vagus nerve stimulation (VNS) therapies approved for epilepsy, depression and stroke rehabilitation^{3–6}, Alzheimer's disease⁷, pain⁸, anxiety⁹, tinnitus¹⁰, rheumatoid arthritis¹¹, inflammatory bowel disease¹², heart failure¹³, diabetes¹⁴, obesity¹⁵, and pulmonary hypertension^{16,17}.

A full list of affiliations appears at the end of the paper.  e-mail: szanos@northwell.edu

VNS is typically delivered through epineural cuff electrodes implanted around the cervical nerve trunk (Fig. 1B), where sensory and motor fibers travel inside nerve fascicles¹⁸. Stimulating smaller vagal fibers, such as those innervating the heart, lungs or abdominal viscera may elicit clinically beneficial, desired effects¹⁹. However, currently used bipolar VNS devices strongly activate larger fibers, some of which innervate organs like the larynx and pharynx and result in side effects, e.g., coughing and voice hoarseness, which may lead to sub-optimal dosing and reduced therapeutic efficacy²⁰. Spatially selective VNS, comprising rectangular pulses delivered through multi-contact cuff electrodes (MCEs) has been shown to activate organ-specific fibers asymmetrically and differentially in swine (Fig. 1C)^{21–23}. To the extent that the fascicular and functional organization of the human vagus nerve shares similarities with that of the swine vagus nerve^{24–28}, spatially focused stimulation may be a viable strategy for more selective VNS. However, even with MCEs,

functional selectivity of rectangular pulse stimulation is limited: larger fibers are still activated before smaller fibers, due to their lower activation threshold^{21,22}, and fibers located at the periphery of the trunk are activated before those at the interior of the trunk, due to closer proximity to stimulating contacts²⁹. Despite its potential translational significance, spatial and temporal control of activation of vagal fibers, i.e., fibers mediating specific desired effects vs. side effects, is currently not feasible.

Interferential current stimulation (iCS) was introduced in the 1950s to facilitate muscle strengthening in athletes^{30,31} and has recently regained attention as a method for targeted neuromodulation^{32,33}. iCS of the brain uses separate electrical sources generated from scalp electrodes, with slightly different, high frequencies (in the order of kHz) that, through temporal interference, give rise to lower frequency amplitude modulations (AMs); AMs produce spatially focused activation of neurons

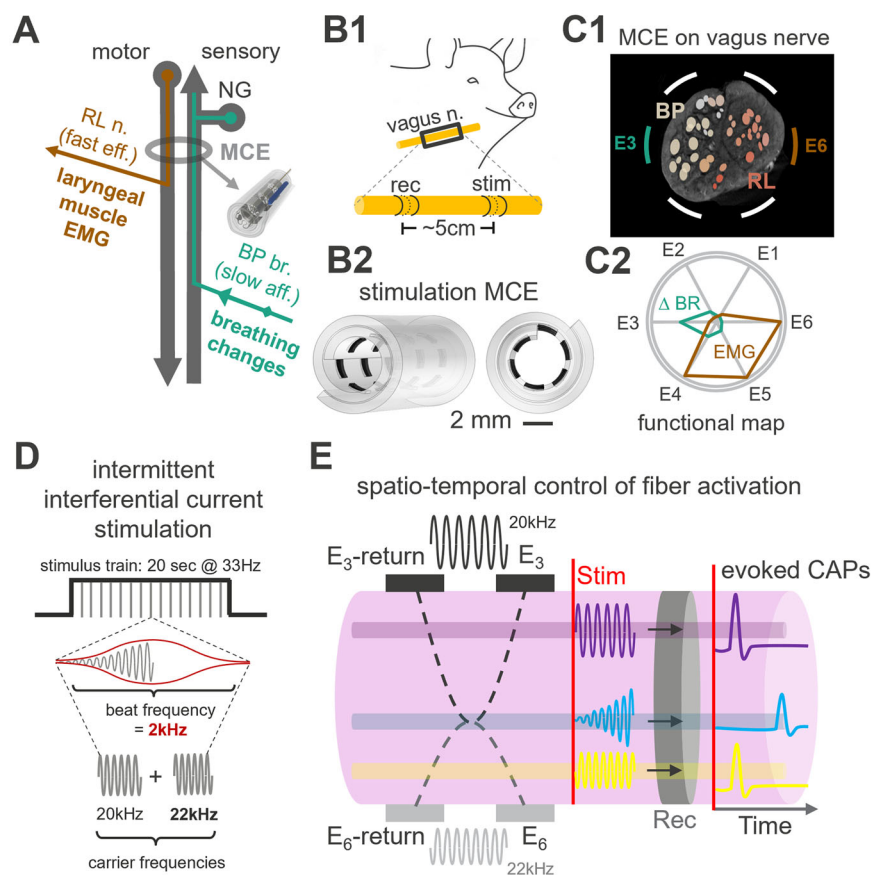


Fig. 1 | Anatomical basis for control of spatiotemporal activation of fibers by vagus nerve stimulation using intermittent, interferential current stimulation (i²CS). **A** Schematic of the vagal trunk: a multi-contact cuff electrode (MCE) is implanted in a swine at the cervical level, at a level below the nodose ganglion (NG). Out of the numerous subpopulations of vagal fibers mediating different physiological functions, shown are fibers relevant to this study, namely fast, motor fibers projecting to laryngeal muscles through the recurrent laryngeal (RL) branch, whose activation produces a laryngeal electromyography (EMG) signal as well as slower, sensory fibers from the lungs, entering the trunk through the bronchopulmonary (BP) branch, whose activation slows down breathing. **B1** Stimulation and recording electrodes placed on the cervical vagus nerve (VN) of a swine used to record evoked nerve potentials and directly assess fiber activation. **B2** Layout of the cylindrical MCE used for VNS, comprising 3 rows of contacts, with 6 contacts in each row. **C1** Schematic cross section of a swine cervical VN with fascicles; fascicle color represents the varying percentages of RL (red) and BP fibers (yellow), determined via post-mortem imaging and fascicle tracking. **C2** Functional mapping of the nerve trunk inferred by single contact stimulation and recording of physiological

responses; contact E3, which is close to BP fascicles, is associated with a strong breathing response (green trace), whereas contact E6, which is close to RL fascicles and located opposite contact E3, is associated with a strong laryngeal EMG response (red trace). **D** i²CS waveform in a 20 s-long stimulus train, with pulse repetition frequency of 33 Hz. Each “pulse” is generated by sinusoidal stimuli with slightly different carrier frequencies (20 and 22 kHz), delivered through separate contacts, which result in amplitude modulation of the short bursts with a beat frequency of 2 kHz (red) through temporal interference. **E** Illustration of the delivery of 2 high frequency sinusoidal stimuli, one between contact E3 and E3-return, and one between contact E6 and E6-return, to produce interference at a specific location inside the nerve trunk. Points close to contacts E3 and E6 do not experience interference or electric field amplitude modulation (AM); the respective fibers (purple and yellow) are activated immediately upon onset of stimulation, resulting in relatively large evoked compound action potentials (CAPs) with short latencies. Areas at the focus of interference experience field amplitude modulation, and the respective fibers (blue) are activated to a lesser degree and only after a delay, resulting in smaller evoked CAPs with longer latencies.

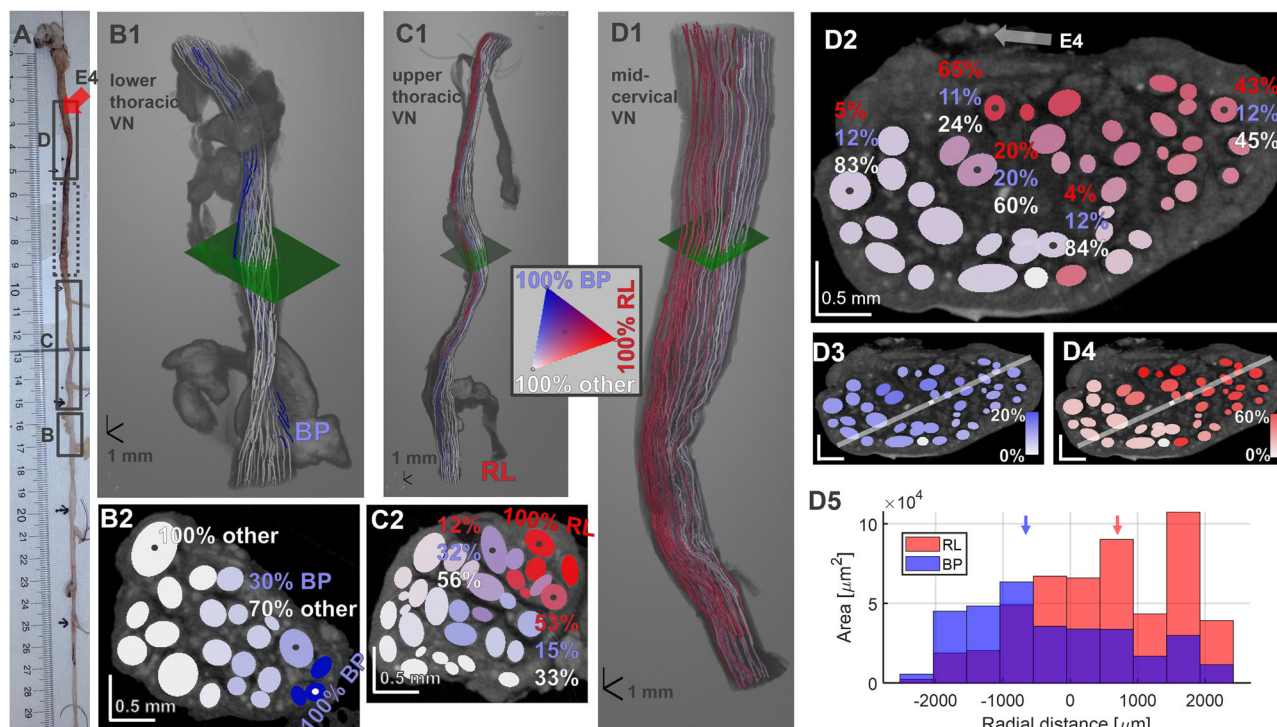


Fig. 2 | Bronchopulmonary- and recurrent laryngeal-specific fascicles progressively merge and give rise to a bimodal anatomical organization at the cervical level. **A** After completion of in vivo experiments, the stimulated nerve, along with the RL and BP branches, was dissected, between the nodose ganglion (rostral) and the lower thoracic region (caudal); the exact location of one of the MCE contacts (E4) was marked on the epineurium of the right, mid-cervical VN with a suture. Each of several segments of the vagal trunk (black rectangles; **B** lower thoracic, **C** upper thoracic; **D** cervical) was imaged with micro-computed tomography (micro-CT), as described previously²². In the micro-CT data, organ-specific fascicles were tracked longitudinally from branch emergence to the mid-cervical level, fascicle splits and merges were identified and percentages of organ-specific fibers in the resulting fascicle(s) were updated according to relative cross-sectional areas of parent and daughter fascicles. **B1** Reconstructed lower thoracic segment with BP branch emergence and respective fascicles shown in blue. **B2** Cross-section of the vagal trunk shown in **B1** (green plane); each fascicle is colored according to the percentage of BP fibers. “Other” vagal fibers are those innervating the heart,

esophagus and abdominal organs. **C1** Same as (**B1**), but for an upper thoracic segment at RL branch emergence, with respective fascicles shown in red. **C2** Fascicular map at the level of the green plane in **C1**. Fascicles contain varying percentages of BP, RL and other fibers, represented using a 3-color scale (inset). **D1** Mid-cervical segment, where the MCE was implanted. **D2** Fascicular map at level of the green plane in **D1**, with location of MCE contact E4 indicated by the suture marking. **D3** Same map as (**D2**), with colormap corresponding to the percentage of BP fibers inside fascicles, normalized between maximum and minimum. Diagonal line approximately corresponds to the radial direction defined by 2 of the contacts of the MCE, the ones used for i²CS in preceding in vivo experiments (E3 and E6). **D4** Percentage of RL fibers (normalized) inside nerve fascicles. **D5** Distribution of estimated BP and RL fiber counts projected on the E3–E6 diagonal line, at different distances from the center of the line; blue and red vertical arrows represent the median values of the BP and RL distance distributions (−593 and 547 μm, respectively; $p < 10^{-10}$, Wilcoxon rank-sum test).

located deeper in the brain^{34,35}. The potential of iCS for targeted stimulation of peripheral somatic nerves was recently demonstrated in small animals, both non-invasively³⁶ and using invasive cuff electrodes³⁷. In addition to continuous iCS, recent work demonstrated the use of short bursts, e.g., consisting a few AM cycles, to entrain low frequency activity in deeper brain regions³⁸.

Whether invasive iCS through cuff electrodes has a role in selective stimulation of nerves with complex fascicular structure in general, and of the vagus nerve in particular, is not known. In this paper, we report a method for VNS, termed intermittent interferential current stimulation (i²CS) that delivers short pulses (< 1 ms) of high-frequency stimulation (around 20 kHz), resulting in AMs in the low kHz range. Through a combination of in vivo experiments in anesthetized swine and in silico computational modeling of an anatomically realistic vagus nerve obtained through fascicle tracking, we uncover working principles of the method and demonstrate that i²CS activates organ-specific fibers in a predictable, spatially focused and temporally precise manner. In animal experiments, i²CS has improved selectivity for a desired effect over a side effect compared to equivalent, non-interfering sinusoidal stimulation.

Results

Bronchopulmonary- and laryngeal-specific fascicles progressively merge, resulting in a bimodal anatomical organization at the cervical vagus nerve of a swine

Use of spatially selective VNS to preferentially activate a desired effect, e.g., from the lungs, over a side effect, e.g., from laryngeal muscles, relies on anatomical separation between bronchopulmonary- and laryngeal-specific vagal fibers at the site of electrode implantation. Separation of organ-specific fibers inside fascicles at the cervical vagus nerve of a swine has been qualitatively demonstrated²² but has not been quantified, and therefore anatomical constraints on spatially selective VNS are unknown. To quantify the anatomical separation of fibers, we tracked the longitudinal trajectories of bronchopulmonary (BP) and recurrent laryngeal (RL) fascicles from the level of branch emergence to the cervical region, identified merges and splits of fascicles, and estimated mixing of fibers inside fascicles at different levels (Fig. 2). At branch emergence, and for a few millimeters in the rostral direction, BP- and RL-specific fascicles are spatially almost completely separated from other fascicles (4 mm for BP; 4.6 mm for RL; Fig. 2B, C, respectively). However, at more rostral levels, BP, RL and other fascicles progressively merge, and no fascicles at the cervical

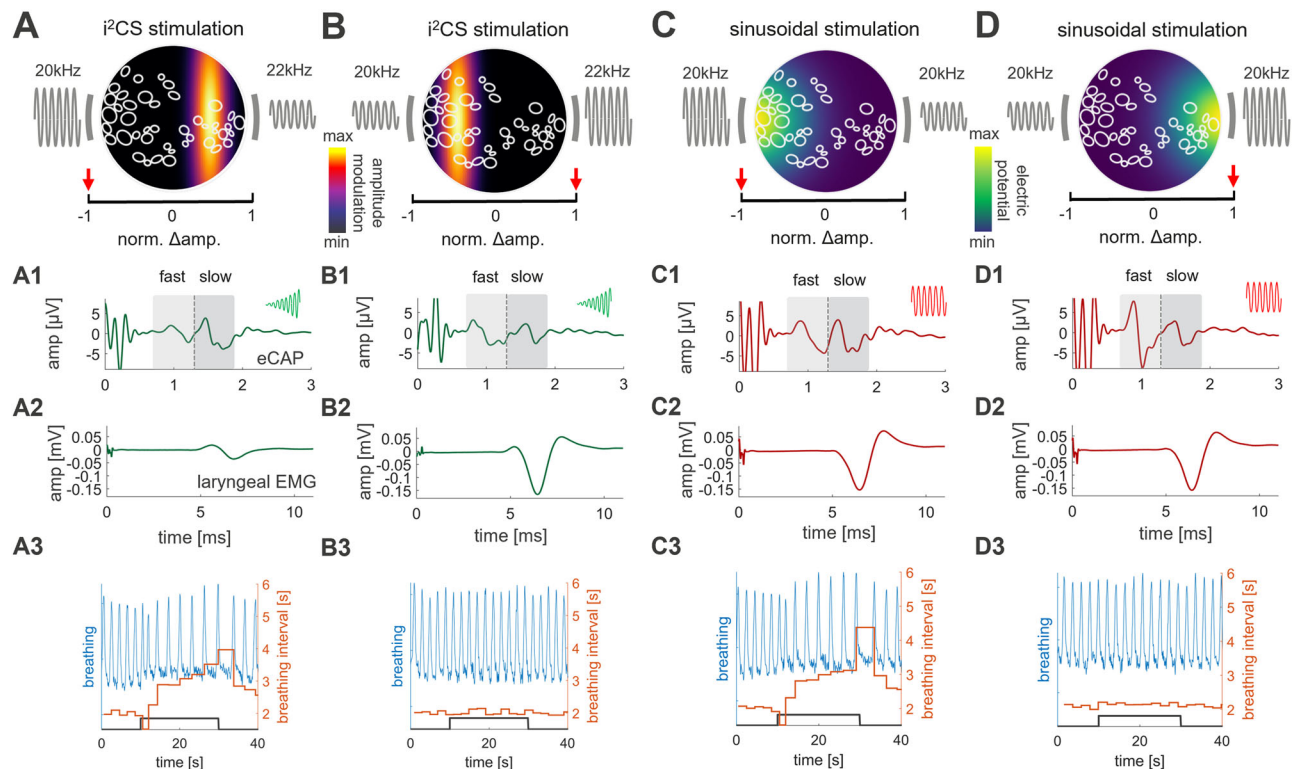


Fig. 3 | i²CS elicits distinct experimental nerve and organ responses that are different than those to equivalent, non-interfering sinusoidal current stimulation.

A Schematic cross section of the stimulated VN of the example animal from Fig. 2 at the level of an implanted MCE; shown are outlines of nerve fascicles and the 2 contacts (grey bars) used for i²CS, with the left source at greater amplitude than the right source (negative steering ratio, expressed as the ratio in amplitude of the left current source with respect to the total current, mapped to a -1 to +1 range for illustration purposes; i.e., 0.9 = -1, 0.7 = -0.5, 0.5 = 0, 0.3 = 0.5, 0.1 = 1. -1 denotes 90% of the total amplitude on the left contact and 10% of the total amplitude on the right contact; red arrow on left side of x-axis); left and right sources have carrier frequencies of 20 kHz and 22 kHz respectively. The colormap represents the maximum peak-to-peak amplitude of the beat interference envelope, indicating the location of the maximal amplitude modulation (cf. Suppl. Fig. S1). **A1** Evoked compound action potential (eCAP) triggered from the onset of i²CS, with 0.75 mA

total current delivered through the 2 sources; slow and fast eCAP components are identified by the shaded areas corresponding to time windows defined by the average conduction velocities for 'slow' and 'fast' fibers. **A2** Weak laryngeal EMG in response to i²CS. **A3** Robust breathing response (blue trace: raw respiratory movements, orange trace: respective breathing interval), during a 20s-long train of i²CS (black trace). **B** Same as in **A**, but for i²CS steered in the opposite direction (i.e., towards the right side; shown are sizeable eCAP and EMG responses, with minimal breathing response). **C** Same as in **A**, but for sinusoidal stimulation. The two current sources have the same carrier frequency (20 kHz). The strength of the electric potential generated by this particular current steering ratio is represented by a colormap. Robust fast eCAP and EMG, as well as intense breathing response. **D** Same as in **C**, but for the opposite steering direction. All eCAP and EMG responses shown as averages triggered from $n = 660$ stimuli.

region project solely to branches innervating a single organ; instead, fascicles contain a mix of BP, RL and other fibers (Fig. 2D). Despite significant merging of fascicles, BP and RL fiber percentage estimates show a distinct spatial arrangement: BP-rich fascicles occupy one area of the nerve and RL-rich fascicles a different area (Fig. 2D3, D4). The result is a bimodal distribution of fibers along a transverse axis, with most RL and BP fibers located at approximately 1 mm on either side of the axis mid-point and about 2 mm away from the nerve periphery (Fig. 2D5).

Using quantitative anatomical tracking, we document bimodal anatomical organization of organ-specific fibers in the cervical vagus nerve of a swine, suggesting that focal stimulation along a transverse direction could improve selectivity of VNS.

Interferential stimulation (IS) elicits distinct nerve and organ responses that are different than those of equivalent, non-interfering sinusoidal stimulation

Interfering current sources give rise to electric fields and amplitude modulations at distinct spatial locations that are different than those with equivalent non-interfering stimulation (Suppl. Fig. S1)³³. To test whether interferential VNS activates different areas inside the vagal trunk, thereby engaging different fiber populations, i²CS was delivered

through pairs of contacts of an MCE (see Methods for detailed stimulation parameters); then, evoked compound action potentials (eCAPs) and physiological responses from the lungs and laryngeal muscles were measured in anesthetized swine. i²CS with uneven stimulus intensities results in AM on one side of the nerve (negative steering ratio, expressed as the ratio in amplitude of the left current source with respect to the total current, mapped to a -1 to +1 range for illustration purposes; i.e., 0.9 = -1, 0.7 = -0.5, 0.5 = 0, 0.3 = 0.5, 0.1 = 1; Fig. 3A). The fast-fiber eCAP and the respective, fast-fiber-mediated, laryngeal electromyography (EMG) signal (Fig. 3A1, A2, respectively; Suppl. Fig. S2) are smaller than those in response to i²CS with the opposite steering ratio (Fig. 3B1, B2, respectively; Suppl. Fig. S2). Slow eCAP and respective breathing responses follow the opposite pattern (Fig. 3A3 vs. B3). To test the hypothesis that differential responses depend on interference rather than solely on activation of nearby vagal fibers by the two sinusoidal sources, sinusoidal stimulation with the same frequency and steering ratio was delivered through the same contacts, resulting in large, fast eCAP and EMG responses in both steering conditions (Fig. 3C1–2 and D1–2). On the other hand, breathing responses in the two steering conditions were similar to those with i²CS (Fig. 3, C3, D3, see also Suppl. Fig. S3 for single contact stimulation).

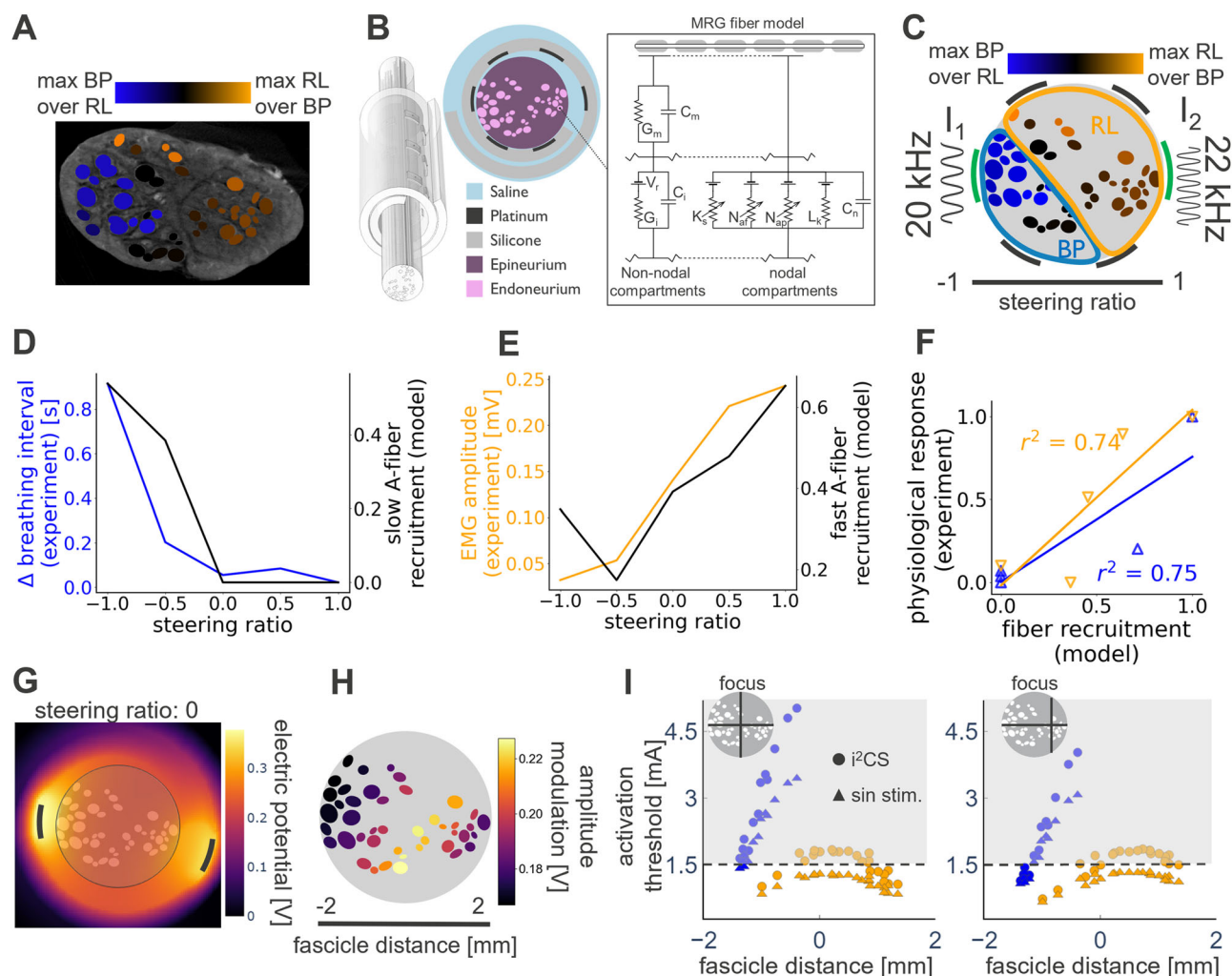


Fig. 4 | An anatomically realistic, physiologically validated biophysical model of the nerve-electrode interface predicts that i²CS produces reduced activation of fibers at the focus of interference. **A** Cross-section of micro-CT-imaged swine vagus nerve at the level of the implanted cuff (same as in Fig. 3). Fascicle color indicates the relative prevalence of BP (blue, maximum 8% more BP) and RL fibers (orange, maximum 50% more RL) within each fascicle. **B** Physical 3D model containing the nerve as an extrusion of the cross-section in **A** and the spiral cuff around it, including the different 3D domain materials (perineurium delimiting each fascicle and surrounding medium not shown) and MRG-model⁸⁴ used to calculate the activation function of each fiber based on the electric field. **C** Cross-section of the nerve model after circular deformation, including the relative placement of (longitudinally positioned pairs of) contacts within the cuff (black lines); the circumferential position of 2 pairs of contacts used for stimulation are highlighted in green. One pair of contacts delivers a 20 kHz and the second a 22 kHz sinusoidal carrier. The horizontal axis represents the ratio in stimulus amplitudes between the 2 contacts that controls the location of the interference focus (steering ratio). For visual clarity, areas with a predominance of RL (or BP) fibers are highlighted. **D** Modeled slow A-fiber (6 μ m) responses to i²CS with different steering ratios (with

a combined total current amplitude of 1.5 mA) and change in breathing rate measured experimentally upon i²CS with the same steering ratios. **E** Modeled fast A-fiber (10 μ m) responses and experimentally recorded EMG responses. **F** Correlation between modeled normalized fiber firing probabilities and normalized physiological responses obtained experimentally in the same animal: fast A-fibers vs. EMG (orange), slow A-fiber vs. breathing response (blue). See Suppl. Fig. S5 for sinusoidal stimulation for **D–F**. **G** Map of the electric potential magnitude generated by i²CS with a total injected current of 1 mA and steering ratio of 0, focusing the amplitude modulation (AM) in the middle of steering axis. **H** Level of AM for all nerve fascicles under the same stimulation conditions in **G**. **I** Fiber activation threshold for i²CS (circles) and for equivalent sinusoidal stimulation (triangles) at BP (blue) and RL (orange) fascicles at different distances from the middle of steering axis for current steering towards the middle of the nerve (left panel) and towards the right side (right panel). Insets indicate the focus of the interferential stimulation with a black cross, dotted black line indicates the current used for computational model that replicates experimental results (1.5 mA), and grey area indicates no activation.

Experimental results suggest that interferential stimulation elicits specific nerve responses that depend on current steering and are different than those elicited by equivalent, non-interfering, sinusoidal stimulation delivered through the same contacts.

Interferential stimulation elicits reduced fiber activation at the focus of interference, in an anatomically realistic, physiologically validated model of the swine vagus nerve

To demonstrate interference at a focal area of the nerve, fiber activity within anatomically characterized organ-specific fascicles needs to be

recorded. Because recording from single fibers was not available to us, we used a recently developed modeling framework³⁹ to compile an anatomically realistic neuro-electric model of a micro-CT-imaged and anatomically quantified swine vagus nerve (Fig. 4A–C). Because the same nerve was stimulated in in vivo experiments, we were able to compare modeled and experimentally measured responses to the same interferential stimuli. For example, the magnitude of the breathing response and the activity of modeled fibers in BP fascicles both change as a function of steering ratio, in a highly correlated manner (Fig. 4D). RL-mediated EMG responses and activity of modeled

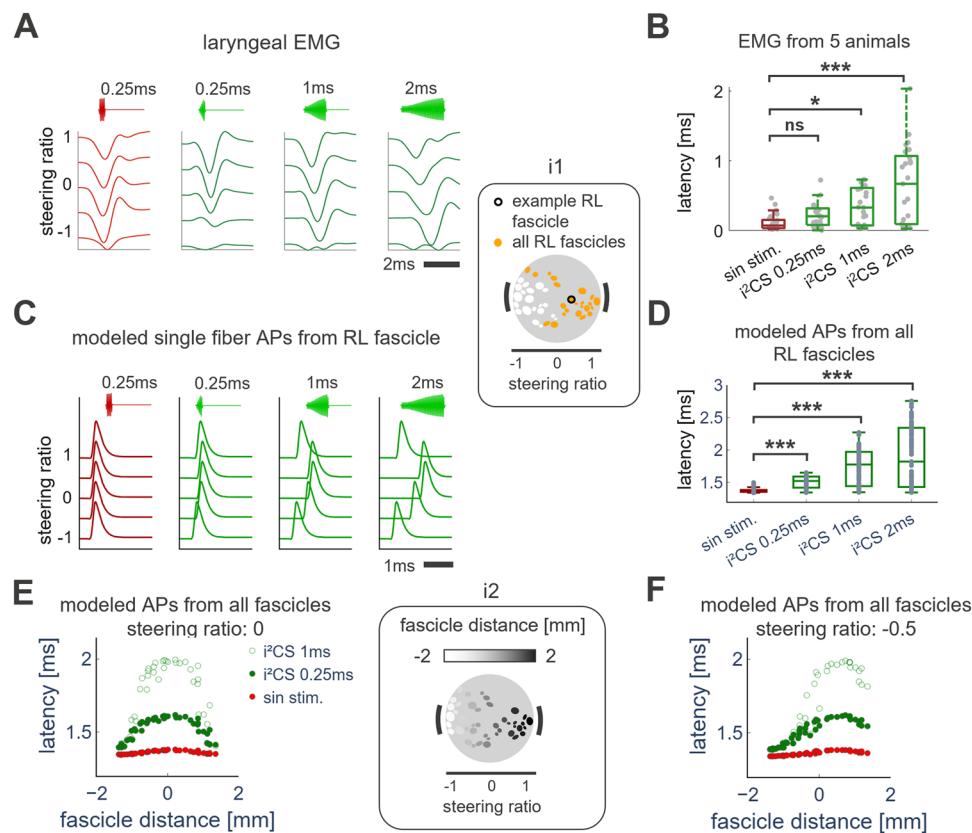


Fig. 5 | Interferential stimulation activates vagal fibers in a specific spatiotemporal pattern, in experiments in swine and in swine vagus nerve models. **A** Example laryngeal EMG responses to a 0.25 ms long sinusoidal stimulus (red) and i²CS (green) at different steering ratios (total amplitude 1 mA) and beat durations (0.25, 1, and 2 ms, from left to right). **B** Difference in latency of onset of laryngeal EMG in response to 0.25 ms-long sinusoidal stimulation (red) and i²CS (green) of different beat durations (0.25, 1, and 2 ms, from left to right), across all steering ratios, in 5 animals. Median response onset latencies to sinusoidal stimulation are shorter compared to i²CS of beat durations of 1 and 2 ms ($p < 0.112$ for sin. stim. vs. i²CS 0.25 ms, $p = 0.024$ for sin. stim. vs. i²CS 1 ms and $p = 0.0002$ for sin. stim. vs. i²CS 2ms, Kruskal–Wallis test). **C** Modeled action potentials (APs) in a fast fiber located in a deep, RL fascicle (black-outlined fascicle in inset i1), in response to sinusoidal (red) and i²CS (green), at different steering ratios (total amplitude 2 mA) and beat durations (0.25, 1 and 2 ms, from left to right), same as those used in **A**.

D Difference in latency of onset of modeled APs calculated from simulations of fast fibers located in all RL fascicles (inset: orange-filled fascicles), for sinusoidal stimulation (red) and i²CS (green), at different beat durations (0.25, 1, and 2 ms, from left to right), across all steering ratios. Median AP latencies to sinusoidal stimulation are shorter compared to i²CS of any beat duration ($p < 0.001$, Kruskal–Wallis test). **E** Onset latency of APs for modeled, fast fibers inside fascicles located at different distances from the middle of the steering axis, in response to sinusoidal stimulation (red data points) or i²CS with beat durations of 0.25 ms (filled green data points) and 1 ms (open green data points); the current was steered at the center of the nerve (steering ratio = 0; total amplitude 2 mA). Inset i2 shows modeled fascicles color-coded according to their distance from the mid-point of the steering axis. **F** Same as **E**, but for a steering ratio of -0.5 (total amplitude 2 mA), resulting in a maximum interferential field on the right side of the nerve cross-section.

RL fibers are similarly correlated (Fig. 4E). Significant correlations between measured physiological responses and modeled fiber responses are found across steering ratios (Fig. 4F), in line with significant correlations between experimental eCAPs and physiological responses, also across steering ratios (Suppl. Fig. S2).

Using the model, we estimated the magnitude of the interferential electric potential (Fig. 4G), the amplitude modulation (AM, Fig. 4H) and the activation thresholds of fibers (Fig. 4I and Suppl. Figs. S4, S21, and S22), within different fascicles. Activation thresholds of fibers located inside fascicles experiencing maximum AM with i²CS are greater than with non-interferential sinusoidal stimulation, indicating reduced fiber activation at the focus of interference (Fig. 4I, left panel). In contrast, for fascicles closer to the nerve periphery, where non-interferential sinusoidal stimulation dominates, activation thresholds are similar for the two stimulation conditions (Fig. 4I, right panel).

Results from anatomically realistic, physiologically validated biophysical models of a swine vagus nerve indicate that i²CS results in increased fiber activation threshold at the focus of interference, compared to equivalent non-interferential stimulation, potentially providing an anatomical basis for selective VNS.

Interferential stimulation activates vagal fibers in a specific spatiotemporal pattern, in experimental recordings and in swine vagus nerve models

The time course of the AM generated with i²CS depends on the difference between the two carrier frequencies, e.g., carrier frequencies of 20 and 22 kHz generate half beats with 0.25 ms duration (Fig. 1D). In principle, the slower rise of AM at the focus of maximum interference should result in gradual depolarization of fibers and a delay in the onset of i²CS-elicited responses, compared to the faster onset responses to sinusoidal stimulation (Fig. 1E). To test this hypothesis, we recorded laryngeal EMG and eCAPs in response to i²CS and sinusoidal stimulation, at different steering ratios and beat durations (Fig. 5A and Suppl. Fig. S6). While sinusoidal stimulation elicits EMG responses with the same short latencies independently of steering ratio, i²CS elicits EMG responses with longer, steering ratio-dependent latencies (Fig. 5A), consistent with a shifting focus of interference. In addition, i²CS with different beat durations elicits EMG responses with different latencies, all of which are longer than the latency of sinusoidal stimulation-elicited responses (Fig. 5B), consistent with slower activation of fibers by the rising AM at the focus of interference.

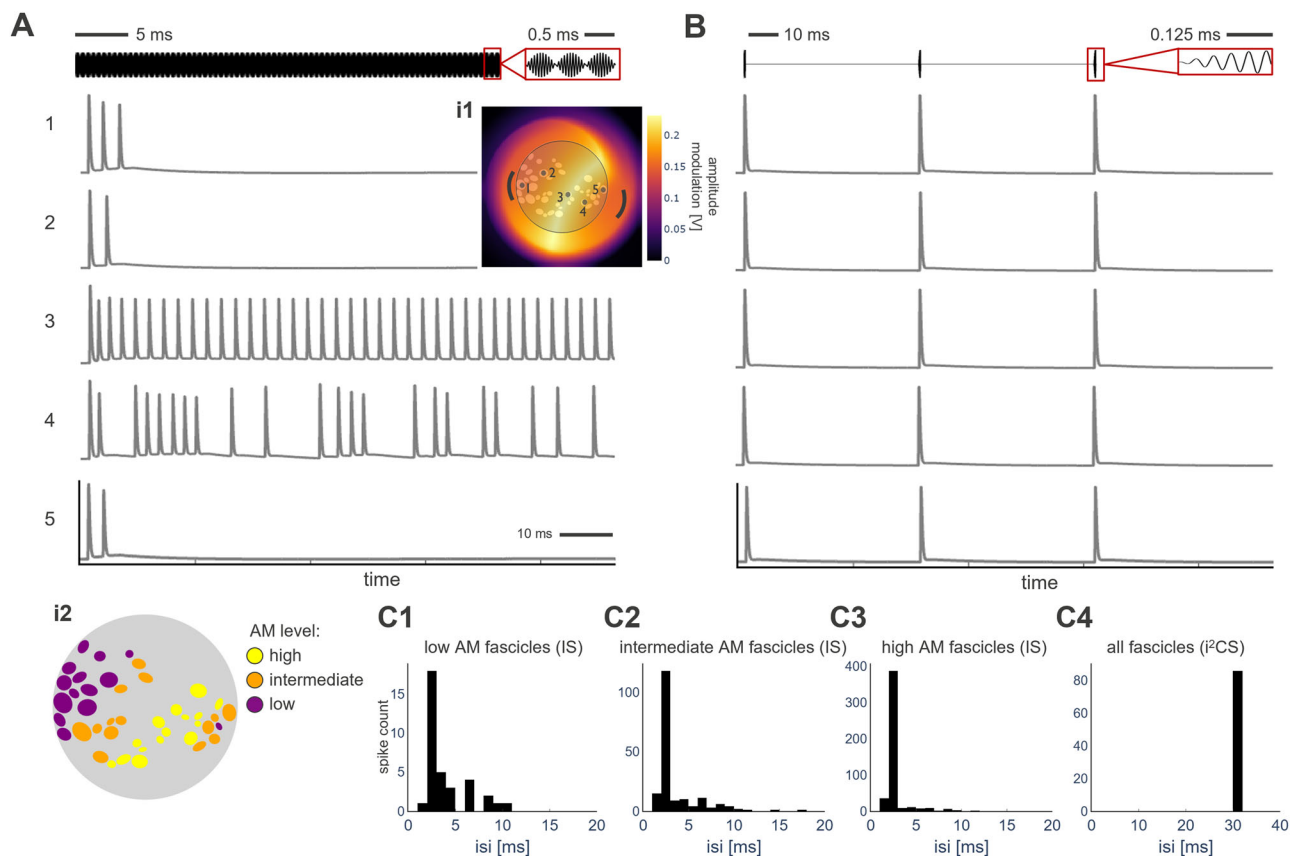


Fig. 6 | Repetition frequency of intermittent interferential stimulation controls timing of evoked action potentials in a temporally precise manner, in models of nerve fibers. A Modeled responses of fast fibers, located in several fascicles, during continuous interferential stimulation (steering ratio = 0). Stimuli with carrier frequencies of 20 kHz and 22 kHz and total amplitude of 2 mA are deployed for 90 ms without interruption: stimulation signal at the top, with inset focusing on 3 consecutive beats. Traces 1–5 show the time course of responses of single fibers inside 5 fascicles, selected to demonstrate the effect of different levels of amplitude modulation (AM) of the electric field. Inset i1 shows the spatial distribution of the AM in a radial cross-section between contacts of each source, where interference is strongest; numbers 1–5 indicate the selected fascicles. Fiber responses range from

activation blocking (fascicles 1, 2, 5), to regular tonic firing (3), to irregular tonic firing (4). **B** Same as (A), but for i^2 CS, demonstrating regular firing in all 5 fascicles, with the inter-spike interval (ISI) being determined by the pulse repetition frequency (in this case 33 Hz, matching in vivo experiments). APs are elicited at different latencies across fascicles (cf. Fig. 5C–F, not all visible here because of long time base). **C1–C4** ISI histograms obtained from APs from fibers in nerve fascicles exposed to different levels of AM (inset i2, fascicles are color-coded based on three ranges of amplitude modulation using quantile values: low <0.33, medium 0.33–0.66, high >0.66), for continuous interferential stimulation (IS): **C1**: fascicles with low AM (below first tertile), **C2**: intermediate AM (between first and second tertile), and **C3**: high AM (above second tertile). **C4**: for i^2 CS (all fascicles).

To establish a single fiber basis for these effects, we modeled action potentials (APs) in response to i^2 CS in a deep-located RL fascicle (inset); we found that APs occur at different latencies, depending on steering ratio, with slower onset of APs at fibers inside vs. outside of the interference focus (Fig. 5C). This finding agrees with experimental results obtained with i^2 CS-elicited eCAPs (Suppl. Fig. S6). Similarly, modeled APs elicited by i^2 CS with longer beat durations occur at longer latencies than those elicited by shorter-beat i^2 CS or with sinusoidal stimulation (Fig. 5C), a difference that holds across all fascicles with a preponderance of RL fibers (Fig. 5D). In modeled fibers, increasing the beat duration of i^2 CS increases the latency of activation of fibers at the focus of interference (Fig. 5E); the same dependency holds for a second interference focus, defined by a different steering ratio (Fig. 5F).

Experimental and modeling results indicate that i^2 CS confers control of spatial and temporal aspects of activation of vagal fibers through selection of current steering and beat duration, respectively.

Intermittent interferential stimulation controls precise timing of action potentials in modeled nerve fibers

Because interference produces a specific spatiotemporal pattern of fiber activation, the choice between continuous or intermittent

stimulation may differentially impact generation of action potentials in nerve fibers. With i^2 CS, fascicles experience a range of AM levels, from minimal AM in superficial fascicles right next to contacts, to maximal AM in deeper fascicles (Fig. 6i1). Modeled responses to continuous interferential stimulation, with the same carrier frequency as i^2 CS used in the in vivo experiments (Fig. 1D), span a variety of profiles after initial onset response, depending on AM at the respective fascicle, e.g., phasic activation followed by a block (Fig. 6A1, A2, and A5), regular tonic (Fig. 6A3) or irregular tonic activation (Fig. 6A4), substantially differing from activation profiles obtained via pure sinusoidal stimulation (Fig. S20), in agreement with previous reports³³. In contrast, i^2 CS with the same carrier frequencies and a pulse duration below the fibers' refractory period (<2 ms), results in a predictable, regular temporal profile of fiber activation characterized only by the onset response, across all fascicles regardless of their location, with an inter-spike-interval (ISI) determined by the pulse repetition frequency (33 Hz; Fig. 6B). Across all nerve fascicles experiencing different levels of AM (Fig. 6i2), the temporal precision of fiber activation, quantified by the variance of ISI distributions, is relatively low for interferential stimulation and depends on the location of the fascicle (Fig. 6C1–C3), whereas it is consistently high for intermittent i^2 CS, independently of the level of AM at the respective fascicle (Fig. 6C4).

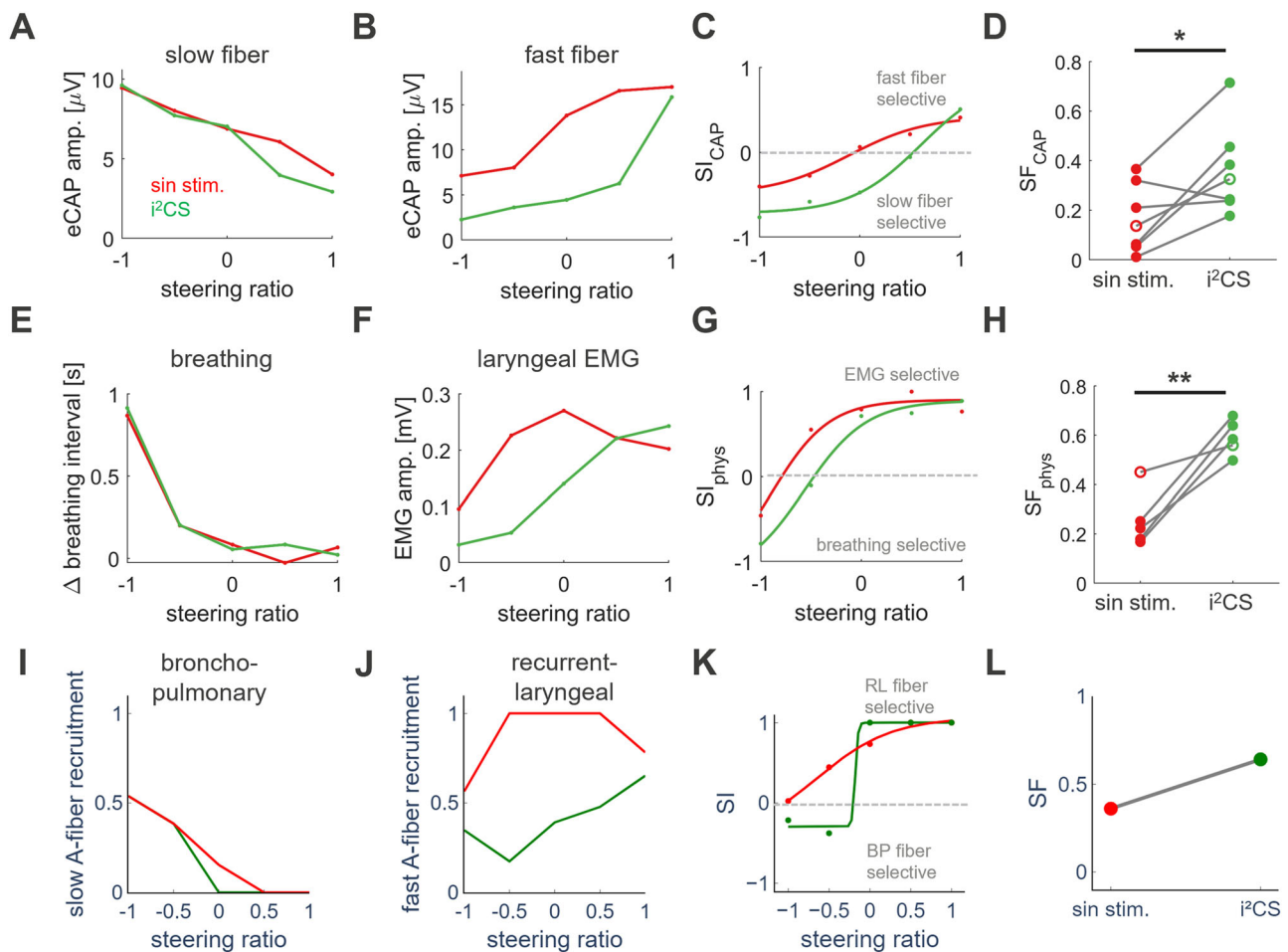


Fig. 7 | Interferential stimulation of the swine vagus nerve attains increased selectivity of a desired effect, mediated by smaller BP fibers, over a side effect, mediated by larger RL fibers, compared to equivalent sinusoidal stimulation. **A** Slow eCAP amplitudes for sinusoidal and interferential stimulation at different steering ratios, from an example animal. **B** Same as in **A**, but for fast eCAPs. **C** Slow over fast eCAP selectivity index (SI) defined as the ratio of the difference over the sum of eCAP amplitudes in **A** and **B** (see Eqs. (2) and (3) in Methods section), fitted with a sigmoidal function, for the 2 stimulus conditions. **D** The mean eCAP selectivity factor (SF), defined as the product of the slope and range of the fitted sigmoidal function of the SI (Suppl. Fig. S9) is significantly different between the 2 stimulus conditions across 7 animals (example animal denoted with open symbols) ($p = 0.038$; Wilcoxon rank-sum test). **E** Magnitude of the (desired) breathing response (change in breathing interval, ΔBI) at different steering ratios, from an example animal, for interferential and equivalent sinusoidal stimulation.

F Amplitude of the (undesired) laryngeal EMG at different steering ratios, in the same animal. **G** Physiological SI, defined as the ratio of the magnitude of the desired over the side effect, in the same animal. **H** The mean physiological SF is significantly different between interferential and equivalent sinusoidal stimulation across 5 animals (open symbols: example animal) ($p = 0.008$, Wilcoxon rank-sum test). **I** Recruitment of BP fibers (modelled as smaller A-fibers, diameter $6 \mu\text{m}$, placed inside fascicles rich in BP fibers) for sinusoidal (red) and interferential (green) stimulation at different steering ratios and a total stimulation amplitude of 1.5 mA . Results obtained using the anatomically realistic biophysical model of the example animal. **J** Same as in **I**, but for RL fibers (modelled as larger A-fibers, diameter $10 \mu\text{m}$, inside fascicles rich in RL fibers). **K** BP over RL SI calculated from the fiber recruitments in **I** and **J**, fitted with a sigmoidal function. **L** SF comparing the sinusoidal and interferential stimulation conditions.

Neural modeling results indicate that intermittent interferential stimulation precisely controls the timing of elicited action potentials in fibers across the entire nerve, with ISIs determined by the pulse repetition frequency.

Interferential stimulation has improved functional selectivity for a desired effect over a side effect compared to equivalent, non-interfering sinusoidal stimulation, in experiments in anesthetized swine

The spatial distributions of RL and BP fibers along a transverse axis of swine vagus nerve show separate peaks at deeper-located fascicles rather than at the nerve periphery (Fig. 2D5). We therefore hypothesized that interferential stimulation producing maximum AM in deeper fascicles on the “RL side” of the nerve would result in reduced activation of an RL-mediated side-effect (laryngeal muscle contraction) over a BP-mediated desired effect (breathing response), compared to

equivalent, non-interfering sinusoidal current stimulation. We recorded nerve potentials (eCAPs) in response to $i^2\text{CS}$ and to sinusoidal stimulation, at different steering ratios; while slow eCAPs, corresponding to the (smaller fiber-mediated) desired effect, are similar in both conditions, $i^2\text{CS}$ elicits smaller fast eCAPs, that correspond to the (larger fiber-mediated) side effect (Fig. 7A, B, respectively). Compared to sinusoidal stimulation, $i^2\text{CS}$ is associated with both greater selectivity and greater range for slow eCAPs across several steering ratios (Fig. 7C), resulting overall in greater selectivity for smaller fibers (Fig. 7D). Furthermore, $i^2\text{CS}$ elicits the same level of breathing response (Fig. 7E), but with smaller magnitude of laryngeal EMG (Fig. 7F), resulting in greater selectivity for desired effect over side effect, both in individual animals and on the population level (Fig. 7D, H, Suppl. Figs. S7, S14–19). Selectivity depends on stimulus intensity: higher stimulation amplitudes tend to reduce selectivity, due to increased fiber recruitment across all fascicles (Suppl. Figs. S30 and S31). When

compared with physiological responses to rectangular pulse stimulation, collected in previously described experiments²², i²CS tends to attain greater selectivity, even though the comparison is not parametric nor systematic and therefore can only be taken as suggestive (Suppl. Fig. S8, note that the experimental design and cuff electrode geometry was different in these experiments).

Consistent with experimental results, recruitment of modeled smaller fibers inside BP fascicles (desired effect) and of larger fibers inside RL fascicles (side effect) depends on steering ratio for i²CS and sinusoidal stimulation (Fig. 7I–K), resulting in different recruitment profiles (Fig. S21) which are consistent with the mechanism of reduced activation at the focus of interference. This is particularly evident for a steering ratio of -0.5 , where the two selectivity profiles are very different from each other, with i²CS being able to achieve better selectivity of BP fibers. This difference results in higher BP fiber selectivity of i²CS over sinusoidal stimulation for a stimulation amplitude of 1.5 mA (Fig. 7L). For high amplitude values, the two waveforms tend to provide similar activation profiles (Suppl. Fig. S21), which is expected due to the increased fiber recruitment at high currents which overcomes the selective steering effect of interference. For reference, computational modeling results obtained with single contact biphasic rectangular wave stimulation delivered close to the BP center (Fig. S23) present a similar selectivity index profile as obtained via i²CS with a steering ratio of -1 .

In a series of experiments in swine, i²CS with interference focus on RL fascicles has improved selectivity for a desired effect, mediated by smaller BP fibers, over a side-effect, mediated by larger RL fibers, compared to equivalent non-interfering sinusoidal stimulation; results are corroborated by modeling studies.

Discussion

Significance of spatially focused and temporally precise control of vagal fiber activation with i²CS

Our study demonstrates that interferential stimulation is a viable method for tunable and precise, spatially focused VNS. Selection of the 2 contact pairs of the MCE defines the steering axis on the radial plane, and of the 2 stimulus intensities (steering ratio) defines the maximum AM site along that axis (Figs. 3–5). To the best of our knowledge, ours is the first demonstration, both in principle and in practice, of precise control of the spatial focus at which the maximum AM of the electric field is generated. To the extent that the vagus nerve in humans has a functional fascicular organization that has similarities with that of the swine vagus nerve, e.g., heart-specific fascicles²⁶, spatial focusing may be a viable strategy for selective VNS¹⁹. This has implications for the future design of more selective VNS devices, since attaining tunable focusing of the electric fields with rectangular pulses delivered through cuff is less feasible. With rectangular pulses, spatial focusing and fiber recruitment depends on the position of stimulated contacts with respect to the underlying spatial distribution of fibers, i.e., the closer the fibers are to the electrode, the lower the activation threshold^{22,40}. Consequently, the only way to improve spatial selectivity of rectangular pulse stimulation is the repositioning of the multi-channel cuff electrodes on the nerve or mechanical deformation of neural tissue to redistribute fiber locations and better expose certain areas in the nerve trunk^{41,42}.

In addition to reducing side effects, more selective VNS may permit testing of a wider range of stimulus intensities for calibration of the desired effect (Fig. 7), potentially resulting in improved dose titration and therapeutic efficacy⁴³. For example, even though VNS in epilepsy is generally safe and well tolerated in the long-run, titration of therapy is performed progressively, over repeated office visits, to minimize side effects like cough and voice alteration, arising from activation of large, low threshold laryngeal and pharyngeal fibers⁴⁴; rapid titration could significantly accelerate clinical response, as reported in a recent meta-analysis⁴⁵. Similarly, in clinical studies of VNS

in heart failure, laryngeal and pharyngeal side effects prevented clinicians from adequately dosing VNS to a level required to activate smaller, higher threshold cardiac fibers mediating the desired effect of cardio-inhibition, possibly contributing to the failure of clinical trials⁴⁶.

Our study also demonstrates that intermittent delivery of short ‘pulses’ of interfering stimuli results in temporally precise activation of vagal fibers, with the timing of elicited APs controlled by the amplitudes and frequencies of the 2 interfering sources (Fig. 5), and ISIs controlled by the pulse repetition frequency (Fig. 6). To the best of our knowledge, i²CS is the first paradigm that combines spatial focusing with temporal precision. Contrary to conduction block observed with continuous kHz stimulation^{47,48}, control of fiber activation is achieved here via an onset response^{49,50}. Conventional, rectangular pulse VNS elicits temporally precise action potentials, time-locked to the stimulus onset, but spatial focusing is limited. Suprathreshold^{51,52} or sub-threshold high-frequency stimulation⁵³ attains improved fiber selectivity but elicits asynchronous action potentials in nerve fibers, with limited temporal precision.

Temporally precise stimulation of vagal fibers may be useful when fiber activation needs to be tightly controlled relative to a dynamically changing physiological state. For example, respiratory-gated auricular nerve stimulation is thought to control hypertension by eliciting afferent volleys at specific phases of the respiratory cycle, i.e., when sensory brainstem neurons involved in the baroreflex are more excitable^{54,55}. Likewise, delivering stimuli to the vagus nerve at specific phases of the cardiac pacemaker cells during the cardiac cycle may differentially impact the risk of vagally-induced sinus, atrial, sinoatrial or ventricular arrhythmias^{56–60}. Finally, closed-loop VNS to control blood pressure⁶¹, treat arrhythmias⁶², modulate gastric sphincter function in gastrointestinal disorders⁶³ or regulate inflammation-related functions of the vagus nerve⁶⁴ relies on delivering responsive stimulation precisely triggered from the detection of a relevant physiological event, a scenario feasible with i²CS.

In terms of hardware viability of i²CS, recent reports have demonstrated feasibility of dedicated, miniaturized and low-power integrated circuits capable of delivering iCS to peripheral nerves⁶⁵ and of methods to efficiently capture and read out neural responses to stimulation⁶⁶. Furthermore, due to intermittent charge delivery, power consumption of i²CS is similar to standard biphasic current stimulators, i.e., i²CS is more power efficient than its continuous counterpart, a property favorable to long-term implanted stimulation devices.

Sources of favorable selectivity and mechanisms of action of i²CS

Interferential stimulation attains reduced levels of a side effect (RL-mediated laryngeal EMG) for similar levels of desired effect (BP-mediated breathing response), compared to equivalent sinusoidal stimulation (Fig. 7E–H). Counterintuitively to our initial expectation that fiber activation would be increased at the focus of interference with i²CS, our experimental and modeling results indicate that i²CS’s favorable response profile is instead driven primarily by a comparatively reduced activation of fibers at the focus of interference. For example, when maximal AM is focused on RL-rich fascicles, laryngeal EMG is reduced, compared to equivalent sinusoidal stimulation, whereas breathing response is comparable (negative steering ratios, Figs. 3 and 7E–H). That is likely caused by reduced activation of larger fibers, some of which innervate the larynx, compared to activation of smaller fibers, some of which innervate the lung (e.g., Fig. 7I, J); this is also reflected in the size of fast and slow eCAPs (e.g., Fig. 7A–D). In contrast, non-interfering sinusoidal stimulation produces less graded laryngeal EMG responses along the steering axis (Fig. 7E–H), as fibers in RL fascicles are now more consistently activated in the absence of AM (Fig. 7I–L). The distribution of fibers inside fascicles can also have a role on this effect, as fascicles predominantly containing RL fibers occupy a larger area within the nerve cross section (Fig. 5 inset i1), meaning that

for every steering ratio, it is more likely that several fascicles containing mainly RL fibers will experience some level of AM, which can therefore result in higher activation thresholds and lower EMG activation for i^2 CS as shown in Fig. 7. Recruitment curves obtained via the computational model demonstrate that i^2 CS achieves generally higher BP fiber selectivity at negative steering ratios, and for a wider range of stimulus intensities (Suppl. Fig. S21).

Although this study did not perform a direct and systematic experimental comparison between single contact rectangular pulse stimulation and i^2 CS, our analysis of historical data obtained in similar experimental conditions²² suggests that i^2 CS may be able to attain improved selectivity for BP-mediated over RL-mediated responses over conventional pulse stimulation (Suppl. Fig. S8). In modeling results, i^2 CS with a steering ratio of -0.5 and no parameter optimization attains similar (maximum) BP fiber selectivity as single contact rectangular stimulation, with 30% less total current delivered from the contact placed close to the BP-rich area (Suppl. Figs. S21 and 23), therefore i^2 CS provides a unique way to compensate for potential suboptimal contact placement and/or movement/drift over time. Additional studies, specifically designed to compare conventional and interferential stimulation waveforms in the same animals and with the same electrodes (shared anatomy and neural interfaces), across a range of stimulus parameters, including intensities, pulse widths, beat and pulsing frequencies, are required to establish improved selectivity of i^2 CS over conventional waveforms.

The different fiber activation profiles between i^2 CS and sinusoidal stimulation likely arise because fibers show lower activation threshold when exposed to a non-amplitude modulated sinusoidal field (20 kHz) compared to an amplitude modulated field (2 kHz beat frequency) (Fig. 4I and Suppl. Fig. S10). The effects of i^2 CS are consistent with a simple threshold mechanism, in which activation of a fiber takes place when the delivered charge results in membrane depolarization that overcomes the activation threshold (Suppl. Fig. S24). This mechanism explains the delayed onset of fiber activation at the focus of interference, as membrane depolarization progressively ramps up with each consecutive cycle, requiring more time to reach the threshold. This is in line with a recent report supporting that interferential stimulation does not rely on envelope extraction for activation, but rather on a simple integration mechanism³⁷.

On the other hand, in kHz-frequency sinusoidal stimulation, the symmetric current cycles, due to nonlinearities in membrane conductivity, produce depolarization cycles that are not fully counter-balanced by the hyperpolarizing periods, resulting in stimulus rectification^{67–69}. For this reason, high frequency bursts facilitate summation of subthreshold stimuli over time, resulting in lower activation thresholds as the number of cycles increases (Gildemeister-effect)^{33,70,71}. In the present work, we deployed a half-beat interferential waveform, which has a total cathodic net charge that is lower than the respective sinusoidal carrier, and a lower charge per cycle due to the presence of a higher frequency component at 22 kHz. This, together with the slower ramp-up of the total charge which has been linked to reduced fiber activation for a given intensity level^{72,73}, would result in increased activation thresholds at the point of interference as compared to the non-interferential case. It should also be noted that, in contrast to previous works that focused on continuous interferential stimulation^{33,37,68}, in the present work we deployed short sinusoidal bursts ($\approx 250 \mu\text{s}$), which impact the activation of fibers differently compared to continuous interferential stimulation (Fig. 6).

Importantly, our experimental and modeling results provide evidence that the anatomical substrate, i.e., organ-specific fibers, upon which spatially selective stimuli are applied, explains a significant amount of variability in the physiological responses, i.e., organ-specific effects (Fig. 4). This underlines the practical significance of resolving the functional anatomy of nerves and using anatomical constraints in the design of nerve interfaces⁷⁴. In our experiments in swine, almost no

electrode pair or steering ratio was associated with perfect selectivity for the desired, BP-mediated breathing effect (Fig. 7D, H). This is likely due to the significant mixing of BP and RL fibers inside the same fascicles (Fig. 2D2–D4) despite an overall organotopic and bimodal distribution of fascicles within the swine vagus nerve^{22,28}, which poses fundamental anatomical limitations in the degree of functional selectivity of any stimulus targeting single fascicles or small groups of fascicles. Attaining better selectivity in the swine nerve or in the possibly less “compartmentalized” human vagus nerve, would likely require even greater stimulus resolution, e.g., by using more than 2 current sources for interference, or high-channel count intraneural electrode arrays that can target smaller sub-fascicular sectors or even single fibers⁷⁵.

Study limitations

Our study has several limitations. First, our methodology for anatomical tracking cannot reconstruct trajectories of single fibers and assumes that mixing of fibers when 2 fascicles merge into one is uniform across the resulting fascicle (Fig. 2). This assumption does not consider sub-fascicular organization of fibers²² and may result in an overestimation of the amount of fiber mixing at the cervical level of a swine. Second, although our models are anatomically realistic and experimentally validated (Figs. 4 and 5), they are not ideal. For example, the nerve in our model is deformed to a circular shape and fascicles are modeled as extrusions of a single nerve cross section instead of more complex splitting and merging structures, thereby limiting accurate modeling of electrical fields⁷⁶. Fiber populations linked to desired and side effects are simplified by modeling a single fiber inside each fascicle with one of two sizes and simplified ionic conductances, instead of modeling many fibers, with a variety of sizes, specific sub-fascicular clustering statistics and a variety of ionic conductances^{22,76,77}. Third, our experimental and modeling approaches do not consider current shunting and escape of current outside of the cuff, both of which are likely altering physiological responses significantly^{21,29}. Experiments performed in anesthetized animals offer limited time to fully explore the stimulation parameter space, hence only selected values of contact pairs, intensities and steering ratios, carrier frequencies and beat frequencies were tested (Suppl. Figs. S30 and 31), preventing us from compiling comprehensive recruitment curves for all stimulation conditions during the experiments. Finally, we did not study i^2 CS delivered through chronically implanted cuffs or in awake animals; stimulation responses in both these cases are likely to be different than those in acutely implanted, anesthetized animals reported here, as shown previously⁷⁸.

In conclusion, in this work, we introduce an electrical stimulation paradigm, termed intermittent interferential current stimulation (i^2 CS), that allows for tunable and precise spatiotemporal control of fiber activation during peripheral nerve stimulation. This paradigm has a favorable selectivity profile for a desired effect over a side effect, compared to equivalent sinusoidal stimulation. We also describe a new mechanism of action of intermittent stimulation, which involves relatively reduced and delayed fiber activation at the focus of interference. Due to its intermittent nature, i^2 CS may be advantageous in terms of energy efficiency, and can be readily implemented in standard implantable stimulation devices.

Methods

Physiology experiments

Animals and surgery. The experimental protocol used in this study has been described in detail earlier²². In brief, the effects of i^2 CS on physiological and neural response were examined in 7 male Yucatan swine (30–54 kg). All animal protocols and surgical procedures were reviewed and approved by the animal care and use committee of Feinstein Institutes for Medical Research and New York Medical College. Animals were sedated with a mixture of Ketamine (10–20 mg/kg) and Xylazine (2.2 mg/kg) or Telazol (2–4 mg/kg). Propofol (4–6 mg/kg, i.v.) was used

to induce anesthesia, and following intubation, the anesthesia was maintained with isoflurane (1.5–3%, ventilation). Body temperature was maintained at 38 and 39 °C using a heated blanket. Blood pressure and blood oxygen level were monitored with a cuff and a pulse oximeter sensor. All surgeries were performed using sterile techniques.

Cervical vagus and laryngeal muscle implants. The right cervical vagus nerve was exposed, and 2 MCEs (Cortec GmbH) were placed on the nerve. The MCE for stimulation (custom AirRay spiral, 18 contacts, see Suppl. Fig. S11) was placed rostrally, ~2 cm away from the nodose ganglion. The design of stimulation MCE aimed at facilitating targeted delivery of IS through minimizing electrode contact size and optimizing its location, which is in accordance with recent recommendation for selective PNS electrode design²¹. A second recording MCE (AirRay helix cuff, 8 recording contacts and 2 ring-shaped reference electrodes) was placed 5–6 cm caudally from the stimulation MCE to record eCAP waveforms. Electrode impedances at a frequency of 1 kHz were measured in vivo using an IMP-2A impedance tester (Microprobe) to verify good contact with the tissue. For laryngeal muscle recordings, Teflon-insulated single or multi-stranded stainless-steel wires were de-insulated at the tip for about 1 mm and inserted in the thyroarytenoid laryngeal muscle with a needle. In 2/7 animals, the laryngeal EMG signal deteriorated and was lost over the course of the experiment, preventing the calculation of physiological selectivity indices (cf. Fig. 7H).

Electrical nerve stimulation. The experimental setup as described in Suppl. Fig. S12 was deployed for in-vivo VNS. Stimulation waveforms and digital signals for timing pulses and stimulation trains were designed using Python 3.9⁷⁹ using a sampling frequency of 1 MHz and transmitted from a PC to a data acquisition (DAQ) board (NI-PCIe6363, National Instruments) via serial communication. The parameters of the two types of stimulation waveforms (sinusoidal and i²CS) are listed in Table 1. Stimuli were presented for 20 s, with a pulse repetition frequency of 33 Hz which was chosen to avoid noise at harmonic multiples of the power line frequency (60 Hz), and low enough to avoid muscle fatigue (cf. Suppl. Fig. S13). Stimulus presentation was randomized and interstimulus interval was 60 s. Stimulation contacts for steering experiments were selected based on an initial functional mapping by stimulating each contact separately at a few amplitudes ranging from 0.5 to 3 mA (Fig. 1C2) using a bipolar configuration. From this mapping, the contact with the lowest threshold for eliciting breathing reduction and an opposing contact were selected. The currents for the steering experiments were chosen around a threshold value (‘medium’ current, see Table 2) that provided an increase in breathing interval (BI) without causing apnea (Table 2). The ‘high’ current condition could, in some cases, still lead to apnea. The ‘steering ratio’ describes the ratio in amplitude of the left current source with respect to the total current as described in Eq. (1), mapped to a –1 to +1 range for illustration purposes; i.e., 0.9 = –1, 0.7 = –0.5, 0.5 = 0, 0.3 = 0.5, 0.1 = 1.

$$\text{current ratio} = \frac{I_1}{I_{\text{tot}}}, \text{ with } I_1 + I_2 = I_{\text{tot}} \tag{1}$$

The choice of a 2 kHz beat frequency for the main comparison with sinusoidal stimulation is related both to the idea of using i²CS as a pulsed technique and to practical setup constraints. One of the main challenges of deploying continuous IS is related to the long (seconds) stimulus durations that are required to generate multiple low frequency beats. This can be a challenge both on the energy consumption in the context of an implant but also on the safety aspects due to the prolonged stimulation. To address these limitations, we have deployed a beat frequency resulting in a total stimulus duration (250 μs) that is comparable to standard rectangular wave pulses (hundreds of μs). Moreover, recording eCAPs requires the stimulus to be shorter than the arrival time of the eCAPs at the recording electrode to avoid stimulation artefact contamination. In our setup, with a typical distance between stimulation and recording electrodes of 5–6 cm, the arrival time of fast eCAPs is around 500 μs after the stimulus onset. Therefore, to keep the stimulation artefact duration less than 500 μs, we used a half-beat of 2 kHz.

The choice of the 20 kHz carrier frequency was driven by the need of having multiple sinusoid cycles within one beat to achieve a good AM of the final interferential signal. In the case of a 250 μs beat, this results in 5 carrier cycles, which creates a well-represented amplitude-modulated interferential signal. On the other hand, choosing a lower carrier frequency, would cause “down sampling” of the final amplitude modulated signal.

The stimulation waveforms were used as input for the DAQ to generate analog output waveforms, and voltage to current conversion was performed via custom-made dual differential Howland current pumps with 1 V: 10 mA conversion factor and power supply of +15/–15 V. To ensure that the stimulation sources were isolated from the rest of the hardware, the Howland current pumps were powered using a 22.5 W, 20000 mAh battery power bank (INIU) and the two outputs of the Howland current source were connected to the stimulation cuff via a custom analog multiplexer designed to allow each independent current source to be routed to any of the electrode channels. The channel selection was controlled digitally using the DAQ system. The connection from the multiplexer to the spiral stimulation cuff was implemented via a micro 360 plastic circular straight tail connector (Omnetics Connector Corporation). DC blocking capacitors were placed at the output of each current pump, and it was verified experimentally using both a resistor network (Fig. S26) and a saline solution (Fig. S27) that no low frequency components were present at the output signal. It was also verified that no electrode polarization occurred at the output electrodes by inspecting the voltage transient during in vitro saline stimulation (Fig. S28), which was also supported by no changes in electrode impedance over repeated experiments (Fig. S29) and no eCAP response changes over the 20 s stimulation period (Fig. S13).

Two additional digital signals were generated by the DAQ: one pulsed digital line whose value was set to 5 V during each stimulation burst and –5 V otherwise, and a stimulation train line whose value was set to 5 V during the whole duration of the stimulation train and 0 otherwise. The two digital lines were directly connected to the digital input ports of the recording instrumentation for synchronization during data acquisition.

Table 1 | Stimulation waveforms for in vivo experiments and computational models

Waveform type	Burst duration [ms]	First carrier frequency [kHz]	Second carrier frequency [kHz]	Pulse repetition frequency [Hz]	Train duration (experiments) [s]
Sinusoidal	0.25	20	20	33	20 (experiment)
i ² CS 0.25 ms	0.25	20	22		0.09 (model)
i ² CS 1 ms	1	20	20.5		
i ² CS 2 ms	2	20	20.25		

Table 2 | Currents used in steering experiments for all animals

Animal #	'Low' current [mA]	'Medium' current [mA]	'High' current [mA]
1 ^a	0.25	0.75 ^b	1.5
2	0.5	0.625 ^b	0.75
3	0.75	1 ^b	1.25
4	0.5 ^b	0.625	0.75
5	0.5	0.6	0.7 ^b
6	0.875	1	1.125 ^b
7	0.425	0.5	0.575 ^b

^adenotes the example animal.^bdenotes the current level used for the population-level comparison.

Recording of physiological and neural signals. All physiological signals were continuously sampled at 1 kHz (PowerLab 16/35, ADI) and visualized using LabChart (ADI). We monitored heart rate (HR) by recording ECG in a 3-lead patch electrode configuration from the wrist of the animal. Signals were amplified using a commercial bio-amplifier (FE238, ADI). Breathing rate was monitored via a respiratory belt transducer (TN1132/ST) connected to a bridge amplifier (FE221, ADI). The train digital line from the DAQ was used to identify the stimulation windows for post-processing.

Neural and EMG signals were sampled at 30 kHz using a second data acquisition system including an amplification and digitization head-stage and controller unit (RHS-32, Intan Tech). The train digital line from the DAQ was used to trigger the start and stop of the recording, and the pulse digital signal was used to identify single burst stimulation windows for post-processing.

Analysis of physiological and neural signals. Raw physiological signals were high-pass filtered post-hoc to remove the DC-component (4-pole Butterworth filter, cut-off frequency: 0.1 Hz) and a custom-made beat-detection algorithm was used to extract the HR and the BI. The increase in BI was used as a measure for stimulation effectiveness since stronger stimulation of the vagus nerve can sometimes lead to apnea, which cannot be quantified via breathing rate reduction. Response strength was calculated as the average BI over the stimulation window (20 s) or until the next breathing cycle in case of apnea, corrected by the average baseline BI in a 10 s window before stimulation onset.

Raw neural signals were averaged over all contacts of the recording cuff (up to 8, excluding channels with no signal/noise) and subjected to a 60 Hz notch-filter implemented either with the Intan recording software or post-hoc in MATLAB. Furthermore, signals were also band-pass filtered post-hoc (4-pole Butterworth filter, high-pass cut-off frequencies: 10 and 260 Hz for EMG and eCAP, respectively; low-pass cut-off frequency: 8000 Hz) before averaging the responses over all stimulus presentations in the train (default: 33 Hz inter-pulse-interval for 20 s, i.e., 660 pulses). EMG response strength was calculated as the peak-to-peak magnitude of the signal in a pre-defined response window after stimulation (4–12 ms). eCAP response strengths were calculated as the peak-to-peak magnitude of the signal in 2 pre-defined response windows after stimulation onset that were derived from conduction velocities of 'fast' and 'slow' A-fibers and the measured distance between the stimulation and recording electrodes (Fast: 55–96 m/s; Slow: 32–55 m/s; Average electrode distance: 5.15 cm). The onset latency of the EMG response was never below ~4 ms in any of the experiments and we limited the analysis of the eCAP response to a window with a maximum of 2 ms.

To quantify the effect of stimulation parameters on fiber and organ functional selectivity, we defined selectivity indexes as previously described⁵¹, adapted to account for the different experimental conditions. The selectivity index *SI* was calculated for eCAP (2) and

physiological (3) responses as follows:

$$SI_{CAP} = \frac{CAP^{fast} - CAP^{slow}}{CAP^{fast} + CAP^{slow}} \quad (2)$$

$$SI_{phys} = \frac{EMG - BI}{EMG + BI} \quad (3)$$

To quantify the dependence of selectivity on steering, the data was fitted with a modified logistic function of the form described in Eq. (4):

$$y = a + \frac{b - a}{1 + \exp^{-k(x - x_0)}} \quad (4)$$

Where *a*, *b*, *k*, and *x*₀ are the minimum and maximum reachable values of the fit, the steepness of the slope and the inflection point, respectively. The Selectivity Factor *SF* was derived from the logistic fits to the *SI*-data as a product of 2 parameters as described in Eq. (5), where *< slope >* and *< range >* are the normalized slope and range of the *SI* sigmoidal function in Eq. (4):

$$SF = \langle slope \rangle \cdot \langle range \rangle \quad (5)$$

The normalized slope is defined as the sigmoid slope converted to degrees and normalized by the maximum value of 90° (Suppl. Fig. S9A). Here, the slope value stands for the 'cutoff sharpness' of the change of selectivity across the nerve diameter while the range describes the maximum relative difference between the activation of one function versus the other. The values for range and slope are reported separately in Suppl. Fig. S9B.

All data analysis was performed using custom-made or publicly available scripts in MATLAB (Mathworks). If not otherwise noted, two-sided Wilcoxon rank-sum tests were used for pair-wise comparisons of means and ANOVA using Kruskal–Wallis tests with Dunn–Sidak correction were used for multiple comparisons of medians. Stars denote *p*-value levels according to **p* < 0.05, ***p* < 0.01 and ****p* < 0.001. Linear regression (least squares) was performed using the 'polyfit' function of MATLAB.

Nerve anatomy

Anatomical dissection and micro-CT imaging of nerve samples. Animals were euthanized by injection of Euthasol (1 ml/10 pounds BW, i.v.); death was confirmed using ECG and absence of arterial pulse. After euthanasia, the right cervical vagus nerve was dissected from above the nodose ganglion to the end of the thoracic region. During that time, nerve branches, still attached to the nerve trunk, were isolated using blunt dissection up to the respective end organ (heart, lung or larynx). A fine suture loop (6–0), radiopaque and therefore visible in micro-CT images, was placed on the epineurium of each branch, close to its emergence from the trunk, to label that branch and maintain a record of the innervated organ during subsequent imaging studies. The nerve trunk, along with organ-specific labels was photographed before and after extraction. The samples were fixed in 10% formalin for 24 h, then transferred to Lugol's solution (Sigma, L6146) for five days to achieve optimal fascicular contrast for the micro-CT scan. Nerve trunks were sectioned into several 6 cm-long segments and the rostral end of each segment was marked with a suture knot, to maintain the rostral-caudal direction. Each nerve segment was scanned individually in the micro-CT scanner. Nerve segments were mounted in position on a vertical sample holder tube. The samples were scanned using Bruker micro-CT Skyscan 1172 with a voxel size of 6 μm, using the following parameters: 55 kV, 149 μA, 0.5 mm Al filter, rotation step of 0.5, and frame averaging of six.

Fascicle reconstruction and tracking. Reconstruction of images was done using cone-beam reconstruction software based on the Feldkamp algorithm (Skyscan NRecon, version 2.2.06), with the following

parameters: ring artifact correction of five, beam hardening correction of 40%, followed by automatic post-alignment. Reconstructed cross-sectional image slices were saved as bitmap files.

The reconstructed image volume was used to manually track the fascicles along the cranial-caudal axis. Ellipses were aligned with the fascicular cross-sections in several image slices. These ellipses were placed on slices approximately 180 microns apart to expedite the labelling process, but this distance was reduced in areas where the fascicles had higher than normal curvature. The parameters of the ellipses were linearly interpolated on the intermediate slices. The centers of the ellipses were connected to form a directed graph where each edge points in the cranial direction, and the graph contains splits or merges where the fascicles split or merge. Because the nerve spans multiple image volumes, these graphs were independently constructed for each image volume and manually joined together.

Fiber mixing model. Each node in the graph was also assigned a tuple representing the percentage of the main trunk, the RL branch, and the BP branch. These structures were manually identified and the leaf nodes in the graph corresponding to these structures were assigned to 100% for the respective structure and 0% of the other structures. The percentages were propagated through the graph from the caudal to the cranial end based on the following rules:

- If a node has only a single input connection from the previous node, then the percentages do not change. This is true even if the previous node branches into multiple nodes. This method assumes homogenous mixing.
- If a node contains multiple input connections from multiple previous nodes, as is the case when merging, then the percentage in the next node is the weighted average of the percentage in the previous nodes with a normalized weighting based on the areas of the previous ellipses. This method assumes instantaneous mixing at merge locations.

Spatial distribution of fibers. The spatial distributions of RL and BP fibers was determined by projecting the centroids of each fascicle onto a line passing through the center of mass for each fiber type. The mass of each fiber type for a given fascicle is proportional to the area of the fascicle times the percentage of each fiber type, assuming a constant fiber density. Histograms of values proportional to the fiber counts for each fiber type were generated along the axis of a diagonal line corresponding to the steering axis (Fig. 2).

Computational modeling

Anatomically realistic 3D computational models were obtained via the adaptation of the ASCENT framework v1.2.2.^{39,80} In this study we deployed the ASCENT framework using Python 3.9, COMSOL Multiphysics 5.6 (COMSOL Inc., Burlington, MA), and NEURON v7.6⁸¹. The framework allows to construct a 3D nerve anatomy starting from an anatomical image and extruding the nerve section over the desired length of the nerve fiber. For this purpose, a nerve cross section from a location right below the middle row of electrodes in the nerve cuff placed on an example animal was selected to generate the 3D model (Suppl. Fig. S11). Binary image inputs were obtained using ImageJ software⁸², and the nerve shape was deformed to account for circular deformation after cuff placement ensuring a minimum inter-fascicle distance and fascicle distance to the nerve perimeter of 10 μm . A scale ratio $\mu\text{m}/\text{pixel}$ of 1.56 was used to account for histological tissue shrinkage and to reach a final nerve diameter of $\approx 3\text{ mm}$ as measured experimentally during the experiment. The conductivity values of all tissues and materials are reported in Table 3. The perineurium was modelled using a thin layer approximation with thickness dependent on the fascicle diameter and whose parameters were derived from pig Vagus nerve experiments²⁷. The perineurium conductivity was selected to be dependent on temperature and frequency, with values set at 37 °C and

Table 3 | Conductivity values for tissues and materials used in the computational model

Element	Conductivity [S/m]	Reference
Perineurium	0.004	83,89
Endoneurium	Anisotropic: x: 0.17 y: 0.17 z: 0.57	89,90
Epineurium	0.158	52,91,92
Medium: saline	1.76	93
Electrode: platinum	9.43×10^6	94
Insulator: silicone	10^{-12}	95

20 kHz to account for the stimulation frequency⁸³. Each fascicle was populated with a single myelinated fiber placed in the middle and modelled using the MRG model^{84,85}, deploying a fiber diameter as detailed in the analysis and a fiber length equal to the nerve length (40 mm).

A 3D model of the electrode cuff placed around the nerve was obtained starting from the electrode geometrical specifications (Suppl. Fig. S11) and placed at the midpoint of the nerve, with a rotation of 90° to replicate contact locations from the experiment. To reduce computational load, only the two pairs (four electrodes) used during the in-vivo experiment were modeled and solved for the electric potentials (Fig. 4C). Material properties were assigned to the different electrode components as follows: electrode contacts (Pt), cuff insulation (silicone), and fill medium and recess (saline). The proximal and outer medium were defined as cylinders with radius 3.5 mm and 4.3 mm respectively, and the outer surface was set to ground. The final model had a total length of 40 mm, a diameter of 8.6 mm and 69772140 mesh elements. Dimensions were deemed appropriate by verifying that doubling separately the nerve length to 80 mm and the diameter to 16 mm would result in activation threshold errors below 2%³⁹.

The voltage transient and activation threshold simulation protocols in ASCENT were used to derive fiber responses resulting from electrical stimulation. As the ASCENT pipeline does not allow to simulate multiple waveforms at the same time as required during i²CS, the framework was extended to support this use case. The extension introduces the summation of the electric potentials resulting from separate simulation waveforms. The electric potential over the 3D space resulting from the injection of a 1 mA DC current is solved separately for each electrode using Laplace's equation, and then modulated by the stimulation waveform, which allows to obtain a temporal profile of the electric potential during stimulation. In the present work, we computed separately the modulated electric potential for each one of the current sources, and then leveraged the principle of superposition of effects to sum the two electric potential temporal profiles, which allowed to obtain a single temporal profile of the electric potential resulting from the presence of two separate current sources. The resulting potential was then used in the pipeline to derive fiber responses. We simulated different stimulation waveforms, replicating the experimental conditions as described in Table 1. For each waveform, the timestep was set to 3 μs , with stimulation starting after 1 ms and with a total stimulation duration of 91 ms.

In the case of continuous IS, the same carrier frequency used for i²CS 0.25 ms (20 kHz and 22 kHz) were used, each carrier having a total duration of 90 ms, which is equivalent to the total duration of the i²CS 0.25 ms stimulus train used for comparison.

For each waveform, a current amplitude of 1.5 mA was used as it best matched experimental data (Suppl. Fig. S25). A current of 2 mA was also used to provide fiber recruitment across all fascicles for large fibers. Moreover, for each current amplitude, five different amplitude ratios were simulated, as defined in (1). For single contact biphasic rectangular wave stimulation, we computed activation thresholds for a

symmetric biphasic rectangular wave with 25 μ s cathodic/anodic pulse widths delivered from a single bipolar contact pair placed close to the BP cluster as depicted in Suppl. Fig. S23.

Analysis of electric potentials. Electric potential maps were generated from COMSOL injecting a 1 mA DC current at each contact and the resulting electric potential at a nerve cross section at the location of the stimulating electrodes was used to generate amplitude maps. For the AM maps, the potential generated by each stimulation source was modulated with a sinusoidal signal with the respective carrier frequency, and the two potentials were then summed together to create a time-varying IS electric potential profile. The resulting signal at each spatial location was processed to extract the magnitude of AM. The absolute value of the Hilbert transform was used to extract the envelope of the signal, and the envelope peak-to-peak amplitude was used to quantify the magnitude of AM. To discretize the amount of AM into three levels (high, intermediate, low), the AM magnitudes at each fascicle location were extracted to generate the values distribution across the whole fascicle population. The three levels were then defined using the values quantiles as follows: low (values below quantile 0.33), intermediate (values between quantiles 0.33 and 0.66) and high (values above quantile 0.66).

Analysis of computational modeling results. The computational modeling outcomes include activation thresholds and voltage transient profiles for each fiber/stimulation parameter combination. This allows to determine the presence of an action potential as a result of electrical stimulation. All analysis on fiber activation was performed using Python 3.9.

To investigate the correlation between physiological responses and fiber activation profiles obtained using the computational model, we performed fascicle clustering based on the percentage of fiber types within each fascicle. We considered all fascicles that contained a majority of BP fibers to be BP fascicles, while fascicles that had a prevalence of RL fibers were assigned to RL.

We computed activation thresholds for fiber diameters of 5, 7, 10, and 12 μ m. The threshold for detecting an action potential was set at -30 mV, the detection location was set to a point placed at 90% of the total fiber length, and the minimum number of action potentials to determine fiber activation was set to 1. We then interpolated activation thresholds using a cubic spline interpolation to obtain activation thresholds for every fiber diameter in the 5–12 μ m range. Based on a distance between the recording and stimulating electrodes of 6 cm, and a time of arrival for fast and slow eCAPs of 0.9 ms and 1.45 ms respectively for the example animal, we calculated conduction speeds of 41 m/s for BP fibers and 66 m/s for RL fibers, which were linked to fiber diameters of 6.6 μ m and 11 μ m respectively⁸⁶. Based on these estimations, we explored fiber diameters of 6 μ m and 7 μ m for BP, and 10 μ m and 11 μ m for RL.

For each of these values and waveform types, the linear correlation with experimental data was computed using the same method described in Fig. 4F for different amplitudes. BP fascicles were populated with a single, slow A-fiber (6 or 7 μ m), while RL fascicles were populated with a single, fast A-fiber (10 or 11 μ m). The knowledge of the function of fibers within the nerve acquired through fiber tracking (see Fig. 2) allowed to simulate the outcome of electrical stimulation on target physiological functions. We considered the generation of an action potential (due to suprathreshold stimulation) for a fiber an indication of the effect on the respective physiological function. We computed the strength of the functional response as the percentage of relevant fibers being activated for a specific physiological function, as described in Eq. (6).

$$\text{Functional Response Modeling}_i = \frac{\sum_{j=1}^{N_i} \text{fiber}_{ij}}{N_i} \quad (6)$$

Here, i indicates the fiber population (BP or RL) with size N_i , and fiber_{ij} is a Boolean value indicating if an action potential was elicited (1) or not (0). The functional response (6) was computed for both sinusoidal and i²CS waveforms with a beat duration of 0.25 ms and for all steering ratios, similarly to in vivo experiments (see Fig. 3). Functional responses obtained through modeling were directly compared with the respective physiological responses obtained experimentally for the same animal during current steering. A linear least-squares regression model was computed between the normalized (min-max normalization into the range of 0 to 1) functional responses obtained through modeling and the respective normalized functional responses obtained experimentally using the `linregress` function from the `scipy.stats` module in Python⁸⁷. Values of 6 μ m and 10 μ m and a stimulation amplitude of 1.5 mA were finally chosen to simulate the responses of slow and fast fibers respectively, as these values provided the best match with experimental data (Suppl. Fig. S25). It should be noted that the stimulation amplitude of 1.5 mA is double the stimulation amplitude used during the experiment (0.75 mA). This disagreement in terms of current amplitudes between model and experiment can be explained by the difficulty in perfectly replicating the experimental conditions in the modelling environment, such as nerve deformation (perfectly circular in the model), distance between stimulating contacts and nerve, and contact impedance. Similar numerical offsets are reported in other modeling literature using the ASCENT framework²¹.

The functional responses derived from modeling were also used to compare the selectivity of sinusoidal stimulation and i²CS using the same approach deployed for experimental data. The functional responses as defined in Eq. (6) obtained at different steering ratios were fitted using a sigmoidal function as described in Eq. (4), and a selectivity factor was computed based on the parameters of the sigmoidal function as detailed in Eq. (5).

To study the fiber activation timing with respect to current steering and waveform type, we performed twofold analysis leveraging the ASCENT voltage transient protocol which allowed to obtain the timings of elicited action potentials. Action potentials were detected in a point located at 10% of the total fiber length and a threshold of -30 mV was selected. Firstly, we considered a single fast A-fiber (10 μ m diameter) placed in a deep fascicle as displayed in Fig. 5, inset i1. A single fiber type was selected to isolate the influence of current steering and waveform type on the timing of action potential. A total stimulation current of 2 mA was selected since it resulted in the generation of an action potential at all steering/waveform combinations. This allowed to study the impact of these stimulation parameters on the timing. Secondly, we considered all the RL-rich fascicles, which were populated with a single fast A-fiber (10 μ m diameter), and we evaluated the activation timing resulting from different waveforms and steering ratios. ANOVA using Kruskal–Wallis test with Dunn–Sidak correction was used for multiple comparisons of medians between waveform types (`scipy.stats.kruskal`⁸⁷ and `scikit_posthocs.posthoc_dunn`⁸⁸ functions in Python). Stars denote p -value levels according to $*p < 0.05$, $**p < 0.01$ and $***p < 0.001$. This experiment was used to compare the laryngeal EMG responses obtained experimentally as a result of different waveforms and steering ratios with the responses obtained using the computational model for the RL-rich fascicles. A stimulation of 1.5 mA was also used to obtain a comparison of the spatiotemporal activation profiles between sinusoidal stimulation and i²CS with different beat frequencies as reported in Fig. S10.

A similar approach was used to investigate the effect of steering/waveform selection on the spatiotemporal activation patterns for all the fascicles in the nerve model. We considered a single fast A-fiber placed in each of the nerve fascicles, during electrical stimulation with a total current of 2 mA. This resulted in most of the fibers being activated at each steering/waveform combination, allowing to investigate the effects of these stimulation parameters on the timing, as shown in Fig. 5.

In the case of continuous stimulation, together with action potential timing analysis, blocking was verified using the blocking threshold protocol available in ASCENT. A 5 nA, 0.1 ms intracellular pulse was delivered after 50 ms from the beginning of the stimulation at one extremity of the nerve (second node from the origin of the nerve in the xyz plane) and the presence of an action potential was verified at the opposite end of the nerve. Blocking thresholds were iteratively searched using the same settings reported for activation thresholds, and blocking of the selected fibers was confirmed if the blocking threshold was below the selected amplitude used to compute voltage transients.

Reporting summary

Further information on research design is available in the Nature Portfolio Reporting Summary linked to this article.

Data availability

The processed experimental data underlying the figures has been published in this repository: <https://doi.org/10.5281/zenodo.14718703>. All data supporting the findings of this study are available within the article and its supplementary files. Any additional requests for information can be directed to, and will be fulfilled by, the corresponding authors. Source data are provided with this paper.

Code availability

The input parameter files and modified code for the modelling framework have been published in the same repository: <https://doi.org/10.5281/zenodo.14718703>.

References

- Jänig, W. *The Integrative Action of the Autonomic Nervous System: Neurobiology of Homeostasis*. <https://doi.org/10.1017/9781108778411> (Cambridge University Press, Cambridge, 2022).
- Karemaker, J. M. The multibranched nerve: vagal function beyond heart rate variability. *Biol. Psychol.* **172**, 108378 (2022).
- Afra, P., Adamolekun, B., Aydemir, S. & Watson, G. D. R. Evolution of the vagus nerve stimulation (VNS) therapy system technology for drug-resistant epilepsy. *Front. Med. Technol.* **3**, 696543 (2021).
- Ben-Menachem, E. Vagus nerve stimulation, side effects, and long-term safety. *J. Clin. Neurophysiol.* **18**, 415–418 (2001).
- Dawson, J. et al. Vagus nerve stimulation paired with rehabilitation for upper limb motor function after ischaemic stroke (VNS-REHAB): a randomised, blinded, pivotal, device trial. *Lancet* **397**, 1545–1553 (2021).
- Sackeim, H. A. et al. Vagus nerve stimulation (VNS™) for treatment-resistant depression: efficacy, side effects, and predictors of outcome. *Neuropsychopharmacology* **25**, 713–728 (2001).
- Merrill, C. A. et al. Vagus nerve stimulation in patients with Alzheimer's disease: additional follow-up results of a pilot study through 1 year. *J. Clin. Psychiatry* **67**, 1171–1178 (2006).
- Chakravarthy, K., Chaudhry, H., Williams, K. & Christo, P. J. Review of the uses of vagal nerve stimulation in chronic pain management. *Curr. Pain. Headache Rep.* **19**, 54 (2015).
- George, M. S. et al. A pilot study of vagus nerve stimulation (VNS) for treatment-resistant anxiety disorders. *Brain Stimul.* **1**, 112–121 (2008).
- Tyler, R. et al. Vagus nerve stimulation paired with tones for the treatment of tinnitus: a prospective randomized double-blind controlled pilot study in humans. *Sci. Rep.* **7**, 11960 (2017).
- Koopman, F. A. et al. Vagus nerve stimulation inhibits cytokine production and attenuates disease severity in rheumatoid arthritis. *Proc. Natl. Acad. Sci. USA* **113**, 8284–8289 (2016).
- Sinniger, V. et al. A 12-month pilot study outcomes of vagus nerve stimulation in Crohn's disease. *Neurogastroenterol. Motil.* **32**, e13911 (2020).
- De Ferrari, G. M. et al. Long-term vagal stimulation for heart failure: eighteen month results from the NEural Cardiac TherApy foR Heart Failure (NECTAR-HF) trial. *Int. J. Cardiol.* **244**, 229–234 (2017).
- Meyers, E. E., Kronemberger, A., Lira, V., Rahmouni, K. & Stauss, H. M. Contrasting effects of afferent and efferent vagal nerve stimulation on insulin secretion and blood glucose regulation. *Physiol. Rep.* **4**, e12718 (2016).
- Pardo, J. V. et al. Weight loss during chronic, cervical vagus nerve stimulation in depressed patients with obesity: an observation. *Int. J. Obes.* **31**, 1756–1759 (2007).
- Ntiloudi, D. et al. Pulmonary arterial hypertension: the case for a bioelectronic treatment. *Bioelectron. Med.* **5**, 20 (2019).
- Zafeiropoulos, S. et al. Ultrasound neuromodulation of an anti-inflammatory pathway at the spleen improves experimental pulmonary hypertension. *Circ. Res.* **135**, 41–56 (2024).
- Upadhye, A. R. et al. Fascicles split or merge every ~560 microns within the human cervical vagus nerve. *J. Neural Eng.* **19**, 054001 (2022).
- Ahmed, U. et al. Strategies for precision vagus neuromodulation. *Bioelectron. Med.* **8**, 9 (2022).
- Zafeiropoulos, S. et al. Vagus nerve stimulation for cardiovascular diseases: is there light at the end of the tunnel? *Trends Cardiovasc. Med.* **34**, 327–337 (2024).
- Blanz, S. L. et al. Spatially selective stimulation of the pig vagus nerve to modulate target effect versus side effect. *J. Neural Eng.* **20**, 016051 (2023).
- Jayaprakash, N. et al. Organ- and function-specific anatomical organization of vagal fibers supports fascicular vagus nerve stimulation. *Brain Stimul.* **16**, 484–506 (2023).
- Thompson, N. et al. Towards spatially selective efferent neuromodulation: anatomical and functional organization of cardiac fibres in the porcine cervical vagus nerve. *J. Physiol.* **603**, 1983–2004 (2025).
- Biscola, N. P. et al. Laterality, sexual dimorphism, and human vagal projectome heterogeneity shape neuromodulation to vagus nerve stimulation. *Commun. Biol.* **7**, 1536 (2024).
- Buyukcelik, O. N. et al. Deep-learning segmentation of fascicles from microCT of the human vagus nerve. *Front. Neurosci.* **17**, 1169187 (2023).
- Kronsteiner, B. et al. Characterization, number, and spatial organization of nerve fibers in the human cervical vagus nerve and its superior cardiac branch. *Brain Stimul.* **17**, 510–524 (2024).
- Pelot, N. A. et al. Quantified morphology of the cervical and sub-diaphragmatic vagus nerves of human, pig, and rat. *Front. Neurosci.* **14**, 601479 (2020).
- Settell, M. L. et al. Functional vagotomy in the cervical vagus nerve of the domestic pig: implications for the study of vagus nerve stimulation. *J. Neural Eng.* **17**, 026022 (2020).
- Nicolai, E. N. et al. Sources of off-target effects of vagus nerve stimulation using the helical clinical lead in domestic pigs. *J. Neural Eng.* **17**, 046017 (2020).
- Ward, A. R. Electrical stimulation using kilohertz-frequency alternating current. *Phys. Ther.* **89**, 181–190 (2009).
- Ward, A. R. & Shkuratova, N. Russian electrical stimulation: the early experiments. *Phys. Ther.* **82**, 1019–1030 (2002).
- Grossman, N. et al. Noninvasive deep brain stimulation via temporally interfering electric fields. *Cell* **169**, 1029–1041.e16 (2017).
- Mirzakhilili, E., Barra, B., Capogrosso, M. & Lempka, S. F. Biophysics of temporal interference stimulation. *Cell Syst.* **11**, 557–572.e5 (2020).
- Acerbo, E. et al. Focal non-invasive deep-brain stimulation with temporal interference for the suppression of epileptic biomarkers. *Front. Neurosci.* **16**, 945221 (2022).
- von Conta, J. et al. Interindividual variability of electric fields during transcranial temporal interference stimulation (tTIS). *Sci. Rep.* **11**, 20357 (2021).

36. Botzanowski, B. et al. Noninvasive stimulation of peripheral nerves using temporally-interfering electrical fields. *Adv. Health. Mater.* **11**, e2200075 (2022).
37. Budde, R. B., Williams, M. T. & Irazoqui, P. P. Temporal interference current stimulation in peripheral nerves is not driven by envelope extraction. *J. Neural Eng.* **20**, 026041 (2023).
38. Wessel, M. J. et al. Noninvasive theta-burst stimulation of the human striatum enhances striatal activity and motor skill learning. *Nat. Neurosci.* **26**, 2005–2016 (2023).
39. Musselman, E. D., Cariello, J. E., Grill, W. M. & Pelot, N. A. ASCENT (Automated Simulations to Characterize Electrical Nerve Thresholds): A pipeline for sample-specific computational modeling of electrical stimulation of peripheral nerves. *PLoS Comput. Biol.* **17**, e1009285 (2021).
40. Sweeney, J. D., Ksienski, D. A. & Mortimer, J. T. A nerve cuff technique for selective excitation of peripheral nerve trunk regions. *IEEE Trans. Biomed. Eng.* **37**, 706–715 (1990).
41. Schiefer, M. A., Polasek, K. H., Triolo, R. J., Pinault, G. C. J. & Tyler, D. J. Selective stimulation of the human femoral nerve with a flat interface nerve electrode. *J. Neural Eng.* **7**, 026006 (2010).
42. Tyler, D. J. & Durand, D. M. Functionally selective peripheral nerve stimulation with a flat interface nerve electrode. *IEEE Trans. Neural Syst. Rehabil. Eng.* **10**, 294–303 (2002).
43. Gorman, P. H. & Mortimer, J. T. The effect of stimulus parameters on the recruitment characteristics of direct nerve stimulation. *IEEE Trans. Biomed. Eng.* **30**, 407–414 (1983).
44. Heck, C., Helmers, S. L. & DeGiorgio, C. M. Vagus nerve stimulation therapy, epilepsy, and device parameters: scientific basis and recommendations for use. *Neurology* **59**, S31–S37 (2002).
45. Tzadok, M. et al. Rapid titration of VNS therapy reduces time-to-response in epilepsy. *Epilepsy Behav.* **134**, 108861 (2022).
46. Gold, M. R. et al. Vagus nerve stimulation for the treatment of heart failure: the INOVATE-HF trial. *J. Am. Coll. Cardiol.* **68**, 149–158 (2016).
47. Kilgore, K. L. & Bhadra, N. Nerve conduction block utilising high-frequency alternating current. *Med. Biol. Eng. Comput.* **42**, 394–406 (2004).
48. Pelot, N. A. & Grill, W. M. In vivo quantification of excitation and kilohertz frequency block of the rat vagus nerve. *J. Neural Eng.* **17**, 026005 (2020).
49. Patel, Y. A. & Butera, R. J. Challenges associated with nerve conduction block using kilohertz electrical stimulation. *J. Neural Eng.* **15**, 031002 (2018).
50. Zhang, X., Roppolo, J. R., de Groat, W. C. & Tai, C. Mechanism of nerve conduction block induced by high-frequency biphasic electrical currents. *IEEE Trans. Biomed. Eng.* **53**, 2445–2454 (2006).
51. Chang, Y.-C. et al. kHz-frequency electrical stimulation selectively activates small, unmyelinated vagus afferents. *Brain Stimul.* **15**, 1389–1404 (2022).
52. Pelot, N. A., Behrend, C. E. & Grill, W. M. Modeling the response of small myelinated axons in a compound nerve to kilohertz frequency signals. *J. Neural Eng.* **14**, 046022 (2017).
53. Vargas, L., Musselman, E. D., Grill, W. M. & Hu, X. Asynchronous axonal firing patterns evoked via continuous subthreshold kilohertz stimulation. *J. Neural Eng.* **20**, 026015 (2023).
54. Garcia, R. G. et al. Modulation of brainstem activity and connectivity by respiratory-gated auricular vagal afferent nerve stimulation in migraine patients. *Pain* **158**, 1461–1472 (2017).
55. Sclocco, R. et al. Respiratory-gated auricular vagal afferent nerve stimulation (RAVANS) effects on autonomic outflow in hypertension. *Annu. Int. Conf. IEEE Eng. Med. Biol. Soc.* **2017**, 3130–3133 (2017).
56. Goto, J., Toyama, J. & Yamada, K. Effects of timing of vagal stimulation on the sinoatrial nodal cell discharge. *J. Electrocardiol.* **16**, 45–52 (1983).
57. Jalife, J., Slenter, V. A., Salata, J. J. & Michaels, D. C. Dynamic vagal control of pacemaker activity in the mammalian sinoatrial node. *Circ. Res.* **52**, 642–656 (1983).
58. Jalife, J. & Moe, G. K. Phasic effects of vagal stimulation on pacemaker activity of the isolated sinus node of the young cat. *Circ. Res.* **45**, 595–608 (1979).
59. Kharbanda, R. K. et al. Vagus nerve stimulation and atrial fibrillation: revealing the paradox. *Neuromodulation* **25**, 356–365 (2022).
60. Slenter, V. A., Salata, J. J. & Jalife, J. Vagal control of pacemaker periodicity and intranodal conduction in the rabbit sinoatrial node. *Circ. Res.* **54**, 436–446 (1984).
61. Zanos, S. Closed-loop neuromodulation in physiological and translational research. *Cold Spring Harb. Perspect. Med.* **9**, a034314 (2019).
62. Ottaviani, M. M., Vallone, F., Micera, S. & Recchia, F. A. Closed-loop vagus nerve stimulation for the treatment of cardiovascular diseases: state of the art and future directions. *Front. Cardiovasc. Med.* **9**, 866957 (2022).
63. Payne, S. C., Furness, J. B. & Stebbing, M. J. Bioelectric neuromodulation for gastrointestinal disorders: effectiveness and mechanisms. *Nat. Rev. Gastroenterol. Hepatol.* **16**, 89–105 (2019).
64. Zanos, T. P. Recording and decoding of vagal neural signals related to changes in physiological parameters and biomarkers of disease. *Cold Spring Harb. Perspect. Med.* **9**, a034157 (2019).
65. Xin, H. et al. A 16-Output 10-V Compliant stimulator ASIC with Sub-10-nA mismatch and simultaneous ETI sensing for selective neural stimulation. *IEEE J. Solid-State Circuits* 1–13 <https://doi.org/10.1109/JSSC.2024.3503914> (2024).
66. He, Y. et al. An implantable neuromorphic sensing system featuring near-sensor computation and send-on-delta transmission for wireless neural sensing of peripheral nerves. *IEEE J. Solid-State Circuits* **57**, 3058–3070 (2022).
67. Neudorfer, C. et al. Kilohertz-frequency stimulation of the nervous system: a review of underlying mechanisms. *Brain Stimul.* **14**, 513–530 (2021).
68. Opančar, A., Ondráčková, P., Trajlinek, J., Đerek, V. & Głowacki, E. D. There is no biophysical distinction between temporal interference stimulation and direct kHz stimulation for actuation of peripheral nerves. Preprint at *bioRxiv* 2024.09.06.611584 <https://doi.org/10.1101/2024.09.06.611584> (2024).
69. Sabah, N. H. Rectification in biological membranes. *IEEE Eng. Med. Biol. Mag.* **19**, 106–113 (2000).
70. Gildemeister, M. Untersuchungen über die Wirkung der Mittel-frequenzströme auf den Menschen. *Pflüger's Arch. Gesamt. Physiol. Menschen Tiere* **247**, 366–404 (1944).
71. Wang, B., Aberra, A. S., Grill, W. M. & Peterchev, A. V. Responses of model cortical neurons to temporal interference stimulation and related transcranial alternating current stimulation modalities. *J. Neural Eng.* **19**, 066047 (2023).
72. Hennings, K., Arendt-Nielsen, L., Christensen, S. S. & Andersen, O. K. Selective activation of small-diameter motor fibres using exponentially rising waveforms: a theoretical study. *Med. Biol. Eng. Comput.* **43**, 493–500 (2005).
73. Vuckovic, A., Tosato, M. & Struijk, J. J. A comparative study of three techniques for diameter selective fiber activation in the vagal nerve: anodal block, depolarizing prepulses and slowly rising pulses. *J. Neural Eng.* **5**, 275–286 (2008).
74. Musselman, E. D., Pelot, N. A. & Grill, W. M. Validated computational models predict vagus nerve stimulation thresholds in preclinical animals and humans. *J. Neural Eng.* **20**, 036032 (2023).
75. Badi, M. et al. Intrafascicular peripheral nerve stimulation produces fine functional hand movements in primates. *Sci. Transl. Med.* **13**, eabg6463 (2021).

76. Ciotti, F. et al. Towards enhanced functionality of vagus neuro-prostheses through in silico optimized stimulation. *Nat. Commun.* **15**, 6119 (2024).
77. Pelot, N. A. et al. Excitation properties of computational models of unmyelinated peripheral axons. *J. Neurophysiol.* **125**, 86–104 (2021).
78. Ahmed, U. et al. Implant- and anesthesia-related factors affecting cardiopulmonary threshold intensities for vagus nerve stimulation. *J. Neural Eng.* **18**, 046075 (2021).
79. Van Rossum, G. & Drake, F. L. *Python 3 Reference Manual* (CreateSpace, Scotts Valley, CA, 2009).
80. Musselman, E. D., Cariello, J. E., Grill, W. M. & Pelot, N. A. *wmglab-duke/ascent: ASCENT v1.2.2*. <https://doi.org/10.5281/zenodo.8298703> (Zenodo, 2023).
81. Hines, M. L. & Carnevale, N. T. The NEURON simulation environment. *Neural Comput.* **9**, 1179–1209 (1997).
82. Schneider, C. A., Rasband, W. S. & Eliceiri, K. W. NIH Image to ImageJ: 25 years of image analysis. *Nat. Methods* **9**, 671–675 (2012).
83. Weerasuriya, A., Spangler, R. A., Rapoport, S. I. & Taylor, R. E. AC impedance of the perineurium of the frog sciatic nerve. *Biophys. J.* **46**, 167–174 (1984).
84. McIntyre, C. C., Richardson, A. G. & Grill, W. M. Modeling the excitability of mammalian nerve fibers: influence of afterpotentials on the recovery cycle. *J. Neurophysiol.* **87**, 995–1006 (2002).
85. McIntyre, C. C., Grill, W. M., Sherman, D. L. & Thakor, N. V. Cellular effects of deep brain stimulation: model-based analysis of activation and inhibition. *J. Neurophysiol.* **91**, 1457–1469 (2004).
86. RUSHTON, W. A. H. A theory of the effects of fibre size in medullated nerve. *J. Physiol.* **115**, 101–122 (1951).
87. Virtanen, P. et al. SciPy 1.0: fundamental algorithms for scientific computing in Python. *Nat. Methods* **17**, 261–272 (2020).
88. Terpilowski, M. A. scikit-posthocs: pairwise multiple comparison tests in Python. *J. Open Source Softw.* **4**, 1169 (2019).
89. Pelot, N. A., Behrend, C. E. & Grill, W. M. On the parameters used in finite element modeling of compound peripheral nerves. *J. Neural Eng.* **16**, 016007 (2019).
90. RANCK, J. B. J. & BEMENT, S. L. The specific impedance of the dorsal columns of cat: an inisotropic medium. *Exp. Neurol.* **11**, 451–463 (1965).
91. Grill, W. M. & Mortimer, J. T. Electrical properties of implant encapsulation tissue. *Ann. Biomed. Eng.* **22**, 23–33 (1994).
92. Stolinski, C. Structure and composition of the outer connective tissue sheaths of peripheral nerve. *J. Anat.* **186**, 123–130 (1995).
93. Horch, K. W. & Kipke, D. R. *Neuroprosthetics: Theory and Practice*. Vol. 8 (World Scientific, 2017).
94. De Podesta, M. *Understanding the Properties of Matter* (CRC Press, 2020).
95. Callister, W. D. Jr & Rethwisch, D. G. *Fundamentals of Materials Science and Engineering: An Integrated Approach* (John Wiley & Sons, 2020).

Acknowledgements

This work was partially supported by NIH SPARC 75N98022C00019 and NIH NINDS-1R01NS136685-01A1, both to S.Z. IMEC has been granted a patent related to this work (patent applicant: Stichting IMEC Nederland; name of inventors: Mark Fichman, Vojkan Mihajlovic; application number: 18/197,335; publication number: US 2023/0364428 A1) that

describes a device for delivering i^2 CS patterns to the neural tissue). The authors wish to thank Patrick van Deursen and Yousef Al-Abed for supporting the collaboration between IMEC and the Feinstein Institutes for Medical Research, Evelien Hermeling for the support on data analysis, and Eva Severijnen for the support on the design of in vivo experimental protocols.

Author contributions

N.R., W.S., P.S., T.D.C., V.M., and S.Z. designed experiments; N.R., W.S., P.S., N.J., D.K., T.D.C., J.W., M.E., K.Q., A.G., M.F.B., and F.L.C. collected data; N.R., W.S., P.S., T.L., and T.D.C. analyzed data; N.R., M.F., T.D.C. developed hardware and/or software; N.R., W.S., P.S., T.L., M.F.B., T.D.C., S.Z., and V.M. wrote the paper; S.Z., V.M., and G.L. conceived, supervised and acquired funding for the study.

Competing interests

IMEC has been granted patents related to this work (US18511762, US0017074A1, US0364428A1, US0198109A1). IMEC and Northwell have submitted patents related to this work.

Additional information

Supplementary information The online version contains supplementary material available at <https://doi.org/10.1038/s41467-025-59595-4>.

Correspondence and requests for materials should be addressed to Stavros Zanos.

Peer review information *Nature Communications* thanks Eric Glowacki and the other, anonymous, reviewer(s) for their contribution to the peer review of this work. A peer review file is available

Reprints and permissions information is available at <http://www.nature.com/reprints>

Publisher's note Springer Nature remains neutral with regard to jurisdictional claims in published maps and institutional affiliations.

Open Access This article is licensed under a Creative Commons Attribution-NonCommercial-NoDerivatives 4.0 International License, which permits any non-commercial use, sharing, distribution and reproduction in any medium or format, as long as you give appropriate credit to the original author(s) and the source, provide a link to the Creative Commons licence, and indicate if you modified the licensed material. You do not have permission under this licence to share adapted material derived from this article or parts of it. The images or other third party material in this article are included in the article's Creative Commons licence, unless indicated otherwise in a credit line to the material. If material is not included in the article's Creative Commons licence and your intended use is not permitted by statutory regulation or exceeds the permitted use, you will need to obtain permission directly from the copyright holder. To view a copy of this licence, visit <http://creativecommons.org/licenses/by-nc-nd/4.0/>.

© The Author(s) 2025

¹imec, Eindhoven, Netherlands. ²Institute of Bioelectronic Medicine, Feinstein Institutes for Medical Research and Northwell Health, Manhasset, NY, USA. ³Sant'Anna School of Advanced Study, Pisa, Italy. ⁴Temple University School of Medicine, Philadelphia, PA, USA. ⁵Zucker School of Medicine at Hofstra/Northwell, Hempstead, NY, USA. ⁶Elmezzzi Graduate School of Molecular Medicine, Manhasset, NY, USA. ⁷These authors contributed equally: Nicolò Rossetti, Weiguo Song, Philipp Schnepel. ✉ e-mail: szanos@northwell.edu